

¹ RESEARCH

² **Modelling the cell-type specific mesoscale murine connectome with
3 anterograde tracing experiments**

⁴ **Samson Koelle**^{1,2}, **Dana Mastrovito**¹, **Jennifer D Whitesell**¹, **Karla E Hirokawa**¹, **Hongkui Zeng**¹, **Marina Meila**², **Julie A
5 Harris**¹, **Stefan Mihalas**¹

⁶ ¹ Allen Institute for Brain Science, Seattle, WA, USA

⁷ ²Department of Statistics, University of Washington, Seattle, WA, USA

⁸ **Keywords:** [Connectivity, Cell-type, Mouse]

ABSTRACT

⁹ The Allen Mouse Brain Connectivity Atlas consists of anterograde tracing experiments targeting
¹⁰ diverse structures and classes of projecting neurons. Beyond regional anterograde tracing done in
¹¹ C57BL/6 wild type mice, a large fraction of experiments are performed using transgenic Cre-lines.
¹² This allows access to cell-class specific whole brain connectivity information, with class defined by
¹³ the transgenic lines. However, even though the number of experiments is large, it does not come close
¹⁴ to covering all existing cell classes in every area where they exist. Here, we study how much we can fill
¹⁵ in these gaps and estimate the cell-class specific connectivity function given the simplifying
¹⁶ assumptions that nearby voxels have smoothly varying projections, but that these projection tensors
¹⁷ can change sharply depending on the region and class of the projecting cells.

¹⁸ This paper describes the conversion of Cre-line tracer experiments into class-specific connectivity
¹⁹ matrices representing the connection strengths between source and target structures. We introduce
²⁰ and validate a novel statistical model for creation of connectivity matrices. We extend the

21 Nadaraya-Watson kernel learning method which we previously used to fill in spatial gaps to also fill in
22 a gaps in cell-class connectivity information. To do this, we construct a "cell-class space" based on
23 class-specific averaged regionalized projections and combine smoothing in 3D space as well as in this
24 abstract space to share information between similar neuron classes. Using this method we construct a
25 set of connectivity matrices using multiple levels of resolution at which discontinuities in connectivity
26 are assumed. We show that the connectivities obtained from this model display expected cell-type
27 and structure specific connectivities. We also show that the wild type connectivity matrix can be
28 factored using a sparse set of factors, and analyze the informativeness of this latent variable model.

AUTHOR SUMMARY

29 Large-scale studies have described the connections between areas in multiple mammalian models in
30 ever expanding detail. Standard connectivity studies focus on the connection strength between areas.
31 However, when describing functions at a local circuit level, there is an increasing focus on cell types.
32 We have recently described the importance of connection types in the cortico-thalamic system, which
33 allows an unsupervised discovery of its hierarchical organization. In this study we focus on adding a
34 dimension of connection type for a brain-wide mesoscopic connectivity model. Even with our
35 relatively massive dataset, the data in the cell type direction for connectivity is quite sparse, and we
36 had to develop methods to more reliably extrapolate in such directions, and to estimate when such
37 extrapolations are impossible. This allows us to fill in such a connection type specific inter-areal
38 connectivity matrix to the extent our data allows. While analyzing this complex connectivity, we
39 observed that it can be described via a small set of factors. While not complete, this connectivity
40 matrix represents a a categorical and quantitative improvement in mouse mesoscale connectivity
41 models.

1 INTRODUCTION

42 The mammalian nervous system enables an extraordinary range of natural behaviors, and has
43 inspired much of modern artificial intelligence. Neural connections from one region to another form
44 the architecture underlying this capability. These connectivities vary by neuron type, as well as source
45 cell body location and target axonal projection structures. Thus, characterization of the relationship
46 between neuron type and source and target structure is important for understanding the overall
47 nervous system.

48 Viral tracing experiments - in which a viral vector expressing GFP is transduced into neural cells
49 through stereotaxic injection - are a useful tool for mapping these connections on the mesoscale
50 (Chamberlin, Du, de Lacalle, & Saper, 1998; Daigle et al., 2018; J. A. Harris, Oh, & Zeng, 2012). The GFP
51 protein moves into the axon of the projecting neurons. The long range connections between different
52 areas are generally formed by axons which travel from one region to another. Two-photon
53 tomography imaging can be used to determine the location and strength of the fluorescent signals in
54 two-dimensional slices. These locations can then be mapped back into three-dimensional space, and
55 the signal may then be integrated over area into cubic voxels to give a finely-quantized
56 three-dimensional fluorescence.

57 Several statistical models for the conversion of such experiment-specific signals into generalized
58 estimates of connectivity strength have been proposed (K. D. Harris, Mihalas, & Shea-Brown, 2016;
59 Knox et al., 2019; Oh et al., 2014; ?). Of these, Oh et al. (2014) and Knox et al. (2019) model **regionalized**
60 **connectivities**, which are voxel connectivities integrated by region. The value of these models is that
61 they provide some improvement over simply averaging the projection signals of injections in a given
62 region. However, these previous works only model connectivities observed in wild type mice in which
63 all neuron types were labeled, and so are poorly suited for extension to tracing experiments that
64 induce cell-type specific fluorescence (J. A. Harris et al., 2019). In particular, GFP expression is
65 induced by Cre-recombinase in cell-types specified by transgenic strain. Thus, this paper introduces a
66 **cell class**-specific statistical model to deal with the diverse set of **Cre-lines** described in J. A. Harris et
67 al. (2019), and expands this model to the entire mouse brain. In cortex a large number of transgenic
68 lines were chosen for their laminar specific expression.

69 Our model is a to-our-knowledge novel estimator that takes into account both the spatial position
70 of the labelled source, as well as the categorical cell class. Like the previously state-of-the-art model in
71 Knox et al. (2019), this model predicts regionalized connectivity as an average over positions within
72 the structure, with nearby experiments given more weight. However, our model weighs class-specific
73 behavior in a particular structure against spatial position, so a nearby experiment specific to a similar
74 cell-class is relatively up-weighted, while a nearby experiment specific to a dissimilar class is
75 down-weighted. This model outperforms the model of Knox et al. (2019) based on its ability to predict
76 held-out experiments in leave-one-out cross-validation. We then use the trained model to estimate
77 overall connectivity matrices for each assayed cell class.

78 The resulting cell-type specific connectivity is a directed weighted multigraph which can be
79 represented as a tensor with missing values. We do not give an exhaustive analysis of this data, but do
80 establish a lower-limit of detection, verify several cell-type specific connectivity patterns found
81 elsewhere in the literature, and show that these cell-type specific signals are behaving in expected
82 ways. We also decompose the wild type connectivity matrix into factors representing archetypal
83 connectivity patterns. These components allow approximation of the regionalized connectivity using
84 a small set of latent components.

85 Section 2 gives information on the data and statistical methodology, and Section 3 presents our
86 results. These include connectivities, assessments of model fit, and subsequent analyses. Additional
87 information on our dataset, methods, and results are given in Supplemental Sections 5, 6, and 7,
88 respectively.

2 METHODS

88 We estimate and analyze cell class-specific connectivity functions using models trained on murine
89 brain viral tracing experiments. This section describes the data used to generate the model, the model
90 itself, the evaluation of the model against its alternatives, and the use of the model in creation of the
91 connectivity estimate matrices. It also includes background on the non-negative matrix factorization
92 method used for decomposing the wild type connectivity matrix into latent factors. Additional
93 information about our data and methods are given in Supplemental Sections 5 and 6, respectively.
94

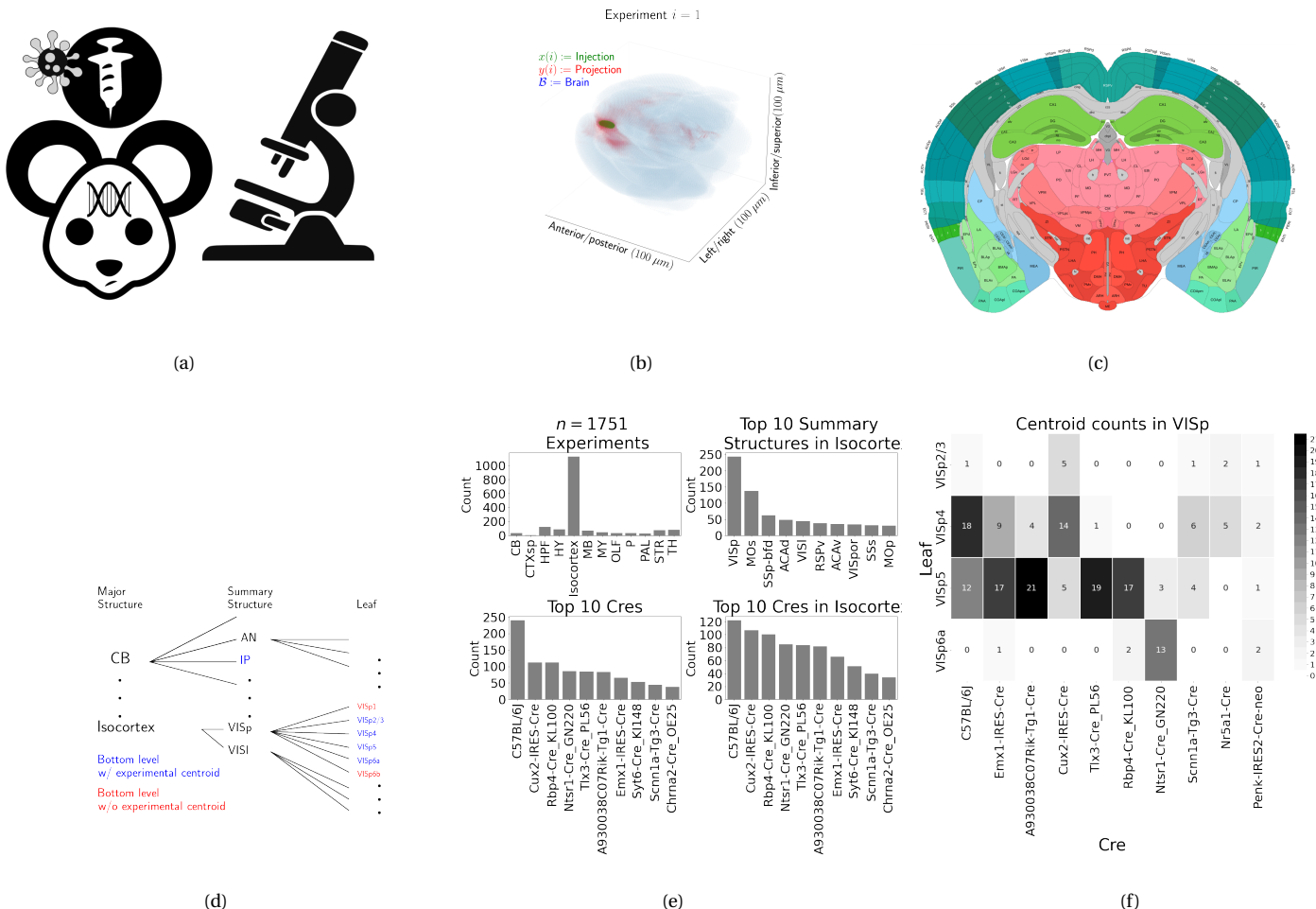


Figure 1: Experimental setting. 1a For each experiment, a Cre-dependent GFP-expressing transgene cassette is transduced by stereotaxic injection into a Cre-driver mouse, followed by serial two-photon tomography imaging. 1b An example of the segmentation of projection (targets) and injection (source) for a single experiment. Within each brain (blue), injection (green) and projection (red) areas are determined via histological analysis and alignment to the Allen Common Coordinate Framework (CCF). 1c Brain region parcellations within a coronal plane of CCFv3. 1d Explanation of nested structural ontology highlighting various levels of CCFv3 structure ontology. Lowest-level (leaf) structures are colored in blue, and structures without an injection centroid are colored in red. 1e Abundances of tracer experiments by Cre-line and region of injection. 1f Co-occurrence of layer-specific centroids and Cre lines within VISp.

95 **Data**

96 (SK's comment:Update figure to show layer and leaf)

97 Our dataset \mathcal{D} consists of $n = 1751$ publicly available murine brain viral tracing experiments from
 98 the Allen Mouse Brain Connectivity Atlas. Figure 1a summarizes the experimental process used to
 99 generate this data. In each experiment, a mouse is injected with an adeno-associated virus (AAV)
 100 encoding green fluorescent protein (GFP) into a single location in the brain. Location of fluorescence
 101 is mediated by the location of the injection, the characteristics of the transgene, and the genotype of
 102 the mouse. In particular, Cre-driver mice are engineered to express Cre under the control of a specific
 103 and single gene promoter. This localizes expression of Cre to regions with certain transcriptomic
 104 cell-types signatures. In such Cre-driver mice, we used a double-inverted floxed AAV to produce
 105 fluorescence that depends on Cre expression in infected cells. To account for the complex cell-type
 106 targeting induced by a particular combination of Cre-driver genotype and GFP promoter, we refer to
 107 the combinations of cell-types targeted by a particular combination of AAV and Cre-drive mice as
 108 cell-classes. For example, we include experiments from Cre-driver lines that selectively label cell
 109 classes located in distinct cortical layers or other nuclei across the whole brain. By our definition, wild
 110 type mice transduced with constitutively active GFP promoters induce fluorescence of a particularly
 111 broad cell class.

112 For each experiment, the fluorescent signal imaged after injection is aligned into the Allen
 113 Common Coordinate Framework (CCF) v3, a three-dimensional average template brain that is fully
 114 annotated with regional parcellations ?. The whole brain imaging and registration procedures
 115 described in detail in Oh et al. (2014); ? produce quantitative metrics of fluorescence discretized at the
 116 $100 \mu\text{m}$ voxel level. Given an experiment, this image was histologically segmented by an analyst into
 117 *injection* and *projection* areas corresponding to areas containing somas, dendrites and axons or
 118 exclusively axons of the transfected neurons. An example of a single experiment rendered in 3D is
 119 given in Figure 1b. Given an experiment i , we represent injections and projections as functions
 120 $x(i), y(i) : \mathcal{B} \rightarrow \mathbb{R}_{\geq 0}$, where $\mathcal{B} \subset [1 : 132] \times [1 : 80] \times [1 : 104]$ corresponds to the subset of the
 121 $(1.32 \times 0.8 \times 1.04)$ cm rectangular space occupied by the standard voxelized mouse brain. We also
 122 calculate injection centroids $c(i) \in \mathbb{R}^3$ and regionalized projections $y_{\mathcal{T}}(i) \in \mathbb{R}^T$ given by the sum of $y(i)$

123 in each region. A detailed mathematical description of these steps, including data quality control, is
124 given in Supplemental Section 6.

125 Our goal is the estimation of **regionalized connectivity** from one region to another. A visual
126 depiction of this region parcellation for a two-dimensional slice of the brain is given in Figure 1c. All
127 structures annotated in the CCF belong to a hierarchically ordered ontology, with different areas of the
128 brain are parcellated to differing finer depths within a hierarchical tree. We denote the main levels of
129 interest as major structures, summary structures, and layers. Not every summary structure has a layer
130 decomposition within this ontology, so we typically consider the finest possible regionalization - for
131 example, layer within the cortex, and summary structure within the thalamus, and denote these
132 structures as leafs. As indicated in Figure 1d, the dataset used to generate the connectivity model
133 reported in this paper contains certain combinations of region and cell class frequently, and others
134 not at all. A summary of the most frequently assayed cell classes and structures is given in Figures 1e
135 and 1f. Since users of the connectivity matrices may be interested in particular combinations, or
136 interested in the amount of data used to generate a particular connectivity estimate, we present this
137 information about all experiments in Supplemental Section 5.

138 ***Modeling Regionalized Connectivity***

Cell-class specific connectivity $f : \mathcal{V} \times \mathbb{R}^3 \times \mathbb{R}^3 \rightarrow \mathbb{R}_{\geq 0}$ gives the directed connection of a particular cell class from one position in the brain to another. In contrast to Knox et al. (2019), which only uses wild type C57BL/6J mice, our dataset has experiments targeting $V = 114$ different combinations of Cre-driver mice and Cre-regulated AAV transgenes jointly denoted as $\mathcal{V} := \{v\}$. As in Knox et al. (2019), we ultimately estimate an integrated regionalized connectivity defined with respect to a set of $S = 564$ source leafs $\mathcal{S} := \{s\}$ and $T = 1123$ target leafs $\mathcal{T} := \{t\}$, of which $1123 - 564 = 559$ are contralateral. That is, we define

$$\text{regionalized connectivity strength } \mathcal{C} : \mathcal{V} \times \mathcal{S} \times \mathcal{T} \rightarrow \mathbb{R}_{\geq 0} \text{ with } \mathcal{C}(v, s, t) = \sum_{l_j \in s} \sum_{l_{j'} \in t} f(v, l_j, l_{j'}),$$

$$\text{normalized regionalized connectivity strength } \mathcal{C}^N : \mathcal{V} \times \mathcal{S} \times \mathcal{T} \rightarrow \mathbb{R}_{\geq 0} \text{ with } \mathcal{C}^N(v, s, t) = \frac{1}{|s|} \mathcal{C}(v, l_j, l_{j'}),$$

$$\text{normalized regionalized projection density } \mathcal{C}^D : \mathcal{V} \times \mathcal{S} \times \mathcal{T} \rightarrow \mathbb{R}_{\geq 0} \text{ with } \mathcal{C}^D(v, s, t) = \frac{1}{|s||t|} \mathcal{C}(v, l_j, l_{j'})$$

139 where l_j and $l_{j'}$ are the locations of source and target voxels, and $|s|$ and $|v|$ are defined to be the
 140 number of voxels in the source and target structure, respectively. Since the normalized strength and
 141 densities are computable from the strength via a fixed normalization, our main statistical goal is to
 142 estimate $\mathcal{C}(v, s, t)$ for all v, s and t . In other words, we want to estimate matrices $\mathcal{C}_v \in \mathbb{R}_{\geq 0}^{S \times T}$. We call this
 143 estimator $\hat{\mathcal{C}}$.

Construction of such an estimator raises the questions of what data to use for estimating which connectivity, how to featurize the dataset, what statistical estimator to use, and how to reconstruct the connectivity using the chosen estimator. We represent these considerations as

$$\hat{\mathcal{C}}(v, s, t) = f^*(\hat{f}(f_*(\mathcal{D}(v, s))). \quad (1)$$

144 This makes explicit the data featurization f_* , statistical estimator \hat{f} , and any potential subsequent
 145 transformation f^* such as summing over the source and target regions. Denoting \mathcal{D} as a function of v
 146 and s reflects that we consider using different data to estimate connectivities for different cell-classes
 147 and source regions. Table 1 reviews estimators used for this data-type used in previous work, as well
 148 as our two main extensions: the Cre-NW and **Expected Loss** (EL) models. Additional information on
 149 these estimators is given in Supplemental Section 6.

Name	f^*	\hat{f}	f_*	$\mathcal{D}(v, s)$
NNLS (Oh et al., 2014)	$\hat{f}(1_s)$	NNLS(X,Y)	$X = x_{\mathcal{S}}, Y = y_{\mathcal{T}}$	I_m/I_m
NW (Knox et al., 2019)	$\sum_{l_s \in s} \hat{f}(l_s)$	NW(X,Y)	$X = l_s, Y = y_{\mathcal{T}}$	I_m/I_m
Cre-NW	$\sum_{l_s \in s} \hat{f}(l_s)$	NW(X,Y)	$X = l_s, Y = y_{\mathcal{T}}$	$(I_l \cap I_v)/I_m$
Expected Loss (EL)	$\sum_{l_s \in s} \hat{f}(s)$	EL(X, Y, v)	$X = l_s, Y = y_{\mathcal{T}}, v$	I_l/I_m

Table 1: Estimation of \mathcal{C} using connectivity data. The regionalization, estimation, and featurization steps are denoted by f^* , \hat{f} , and f_* , respectively. The training data used to fit the model is given by index set I . We denote experiments with centroids in particular major brain divisions and leafs as I_m and I_l , respectively. Data I_l/I_m means that, given a location $l_s \in s \in m$, the model \hat{f} is trained on all of I_m , but only uses I_l for prediction. The non-negative least squares estimator (NNLS) fits a linear model that predicts regionalized projection signal $y_{\mathcal{T}}$ as a function of regionalized injection signal $x_{\mathcal{S}}$. Thus, the regionalization step for a region s is given by applying the learned matrix \hat{f} to the s -th indicator vector. In contrast, the Nadaraya-Watson model (NW) is a local smoothing model that generates a prediction for each voxel within the source structure that are then averaged to create estimate the structure-specific connectivity.

150 Our contributions - the Cre-NW and Expected Loss (EL) models - have several differences from the
 151 previous methods. In contrast to the non-negative least squares (Oh et al., 2014) and
 152 Nadaraya-Watson (Knox et al., 2019) estimators that account only for source region s , our new
 153 estimators account cell class v . The Cre-NW estimator only uses experiments from a particular class
 154 to predict connectivity for that class, while the EL estimator shares information between classes
 155 within a structure. Both of these estimator take into account both the cell-class and the centroid
 156 position of the experimental injection. Like the NW and Cre-NW estimator, the EL estimator
 157 generates predictions for each voxel in a structure, and then sums them together to get the overall
 158 connectivity. However, in contrast to the NW approaches, the EL estimate of the projection vector for
 159 a cell-class at a location weights the average projection of that cell-class in the region containing the
 160 location against the relative locations of all experimental centroids in the region regardless of class.

161 That is, cell-class and source region combinations with similar average projection vectors will be
162 upweighted when estimating \hat{f} . Thus, all experiments that are nearby in three-dimensional space can
163 help generate the prediction, even when there are few nearby experiments for the cell-class in
164 question. A detailed mathematical description of our new estimator is given in Supplemental Section
165 6. (SK's comment:**cell-class versus Cre-line?**)

166 ***Model evaluation***

167 We select optimum functions from within and between our estimator classes using **leave-one-out**
 168 **cross validation**, in which the accuracy of the model is assessed by its ability to predict projection
 169 vectors experiments excluded from the training data on the basis of their cell class and experimental
 170 centroid. Equation 1 includes a deterministic step f^* included without input by the data. The
 171 performance of $\hat{\mathcal{C}}(v, s, t)$ is thus determined by performance of $\hat{f}(f_*(\mathcal{D}(v, s)))$. Thus, we evaluate
 172 prediction of $f_{\mathcal{T}} : \mathbb{R}^3 \rightarrow \mathbb{R}_{\geq 0}^T$ - the regionalized connection strength at a given location.

173 Another question is what combinations of v , s , and t to generate a prediction for. Our EL and
 174 Cre-NW models are leaf specific. They only generate predictions for cell-classes in leafs where at least
 175 one experiment with a Cre-line targeting that class has a centroid. To accurately compare our new
 176 estimators with less-restrictive models such as used in Knox et al. (2019), we restrict our evaluation set
 177 to Cre driver/leaf combinations that are present at least twice. The sizes of these evaluation sets are
 178 given in Supplemental Section 5.

We use weighted l_2 -loss to evaluate these predictions.

$$\text{l2-loss } \ell(y_{\mathcal{T}}(i)), \widehat{y_{\mathcal{T}}(i)}) := \|y_{\mathcal{T}}(i)) - \widehat{y_{\mathcal{T}}(i)}\|_2^2.$$

$$\text{weighted l2-loss } \mathcal{L}(\widehat{f}(f_*)) := \frac{1}{|\{\mathcal{S}, \mathcal{V}\}|} \sum_{s, v \in \{\mathcal{S}, \mathcal{V}\}} \frac{1}{|I_s \cap I_v|} \sum_{i \in (I_s \cap I_v)} \ell(y_{\mathcal{T}}(i)), \hat{f}_{\mathcal{T}}(f_*(\mathcal{D}(v, s) \setminus i)).$$

179 This is a somewhat different loss from Knox et al. (2019), both because of the normalization of
 180 projection, and because of the increased weighting of rarer combinations of s and v implicit in the
 181 $\frac{1}{|I_s \cap I_v|}$ term in the loss. The establishment of a lower limit of detection and the extra cross-validation
 182 step used in the EL model to establish the relative importance of regionally averaged cell-class
 183 projection and injection centroid position are covered in Supplemental Section 6.

184 ***Connectivity analyses***

185 We examine latent structure underlying our estimated connectome using two types of unsupervised
 186 learning. Our use of hierarchical clustering is standard, and so we do not review it here. However, our
 187 application of non-negative matrix factorization (NMF) to decompose the estimated long-range
 188 connectivity into **connectivity archetypes** that linearly combine to reproduce the observed
 189 connectivity of some independent interest. Non-negative matrix factorization refers to a collection of
 190 **dictionary-learning** algorithms for decomposing a non-negatively-valued matrix such as \mathcal{C} into
 191 positively-valued matrices called, by convention, weights $W \in \mathbb{R}_{\geq 0}^{S \times q}$ and hidden units $H \in \mathbb{R}_{\geq 0}^{q \times T}$.
 192 Unlike PCA, NMF specifically accounts for the fact that data are all in the positive orthant. The matrix
 193 H is typically used to identify latent structures with interpretable biological meaning, and the choice
 194 of matrix factorization method reflects particular scientific subquestions and probabilistic
 195 interpretations.

196 Our algorithm solves the following optimization problem

$$\text{NMF}(\mathcal{C}, \lambda, q) := \arg \min_{W \in \mathbb{R}_{\geq 0}^{S \times q}, H \in \mathbb{R}_{\geq 0}^{q \times T}} \frac{1}{2} \| \mathbf{1}_{d(s,t) > 1500\mu m} \odot \mathcal{C} - WH \|_2^2 + \lambda (\|H\|_1 + \|W\|_1).$$

197 For this decomposition we ignore connections between source and target regions less than $1500\mu m$
 198 apart. This is because short-range projections resulting from diffusion dominate the matrices $\hat{\mathcal{C}}$, and
 199 represent a less-interesting type of biological structure. We set $\lambda = 0.002$ to encourage sparser and
 200 therefore more interpretable components. We use unsupervised cross-validation to determine an
 201 optimum q , and show the top 15 stable components (?). Stability analysis accounts for the
 202 difficult-to-optimize NMF program by clustering the resultant H from multiple replicates. Since the
 203 NMF objective is difficult to optimize and sensitive to initialization, we follow up with a stability
 204 analysis. The medians of the component clusters appearing frequently across NMF replicates are
 205 selected as **connectivity archetypes**. Details of these approaches are given in Supplementary Sections
 206 6 and 7.

3 RESULTS

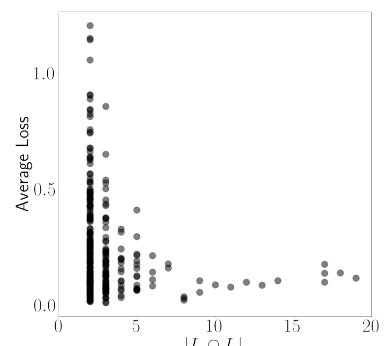
207 We main result of this paper is the collection of cell-type specific connectivity estimates from the Allen
208 Mouse Connectivity Atlas (MCA) experiments. We first establish that our novel expected-loss (EL)
209 estimator performs best in validation assays for estimating wild-type and cell-type specific
210 connectivities. We then show that Cre-specific connectivity matrices generated using this model are
211 consistent with known biology. Finally, we factor some of these connectivity matrices to show how
212 connectivity arises from underlying statistical patterns, and that these may be associated with
213 cell-types.

214 *Model evaluation*

215 In general, our EL model performs better than the other estimators that we consider. Table 5 contains
216 weighted losses from leave-one-out cross-validation of candidate models, such as the NW Major-WT
217 model from Knox et al. (2019). The EL model combines the good performance of class-specific
218 models like NW Leaf-Cre in regions like Isocortex with the good performance of class-agnostic models
219 in regions like Thalamus. Additional information on model evaluation, including class and structure-
220 specific performance, is given in Appendix 5. In particular, Supplementary Table 4 contains the sizes
221 of these evaluation sets in each major structure, and Supplementary Section 7 contains the structure-
222 and class specific losses.

\hat{f}	Mean Leaf-Cre Mean $I_c \cap I_L$	NW Major-Cre NW $I_c \cap I_M$	NW Leaf-Cre NW $I_c \cap I_L$	NW Leaf NW I_L	NW Major-WT NW $I_{wt} \cap I_M$	NW Major NW I_M	EL EL I_L
Isocortex	0.239	0.252	0.234	0.279	0.274	0.274	0.228
OLF	0.193	0.233	0.191	0.135	0.179	0.179	0.138
HPF	0.175	0.332	0.170	0.205	0.228	0.228	0.153
CTXsp	0.621	0.621	0.621	0.621	0.621	0.621	0.621
STR	0.131	0.121	0.128	0.169	0.232	0.232	0.124
PAL	0.203	0.205	0.203	0.295	0.291	0.291	0.188
TH	0.673	0.664	0.673	0.358	0.379	0.379	0.369
HY	0.360	0.382	0.353	0.337	0.317	0.317	0.311
MB	0.168	0.191	0.160	0.199	0.202	0.202	0.159
P	0.292	0.292	0.292	0.299	0.299	0.299	0.287
MY	0.268	0.347	0.268	0.190	0.189	0.189	0.204
CB	0.062	0.062	0.062	0.068	0.112	0.112	0.068

(a)



(b)

Table 2: ?? Losses from leave-one-out cross-validation of candidate models. **Bold** numbers are best for their major structure. ?? Empirical performance of selected EL model by data abundance. The model is more accurate in Cre-leaf combinations where it draws on more data.

223 *Connectivities*

224 Our main result is the estimation of matrices $\hat{\mathcal{C}}_v \in \mathbb{R}_{\geq 0}^{S \times T}$ representing connections of source structures
 225 to target structures for particular Cre-lines v . We confirm the detection of several well-established
 226 connectivities within our tensor, although we expect additional interesting biological processes to be
 227 identifiable. The connectivity tensor and code to reproduce it are available at
 228 https://github.com/AllenInstitute/mouse_connectivity_models/tree/2020.

229 *Overall connectivity* Several known biological projection patterns are evident in the wild-type
 230 connectivity matrix \mathcal{C}_{wt} shown in Figure 2a. This matrix shows connectivity from leaf sources to leaf
 231 targets. Large-scale patterns like intraareal connectivities and ipsilateral connections between cortex
 232 and thalamus are clear, as in previous estimates in J. A. Harris et al. (2019); Knox et al. (2019); Oh et al.
 233 (2014).

234 The layer-specific targeting of the different Cre-lines enables our estimated wild-type connectivities
 235 to resolve at the layer level. This contrasts the model in Knox et al. (2019), which is denominated as
 236 the NW Major-WT model whose accuracy is evaluated in Table 5. Layer-specificity is a major

237 advantage of including distinct Cre-lines. For comparison, we also plot averages over component
238 layers weighted by layer size projections between summary-structure sources and targets in the cortex
239 in Figure 2b. Our connectivities therefore exhibit a finer differentiation between regions than those in
240 Knox et al. (2019) This also enables us to lower our limit of detection and examine a broader range of
241 connectivity strengths. Importantly, as shown in Table 5 this finer spatial resolution corresponds to
242 the increased accuracy of our EL model over the NW Major-WT model.

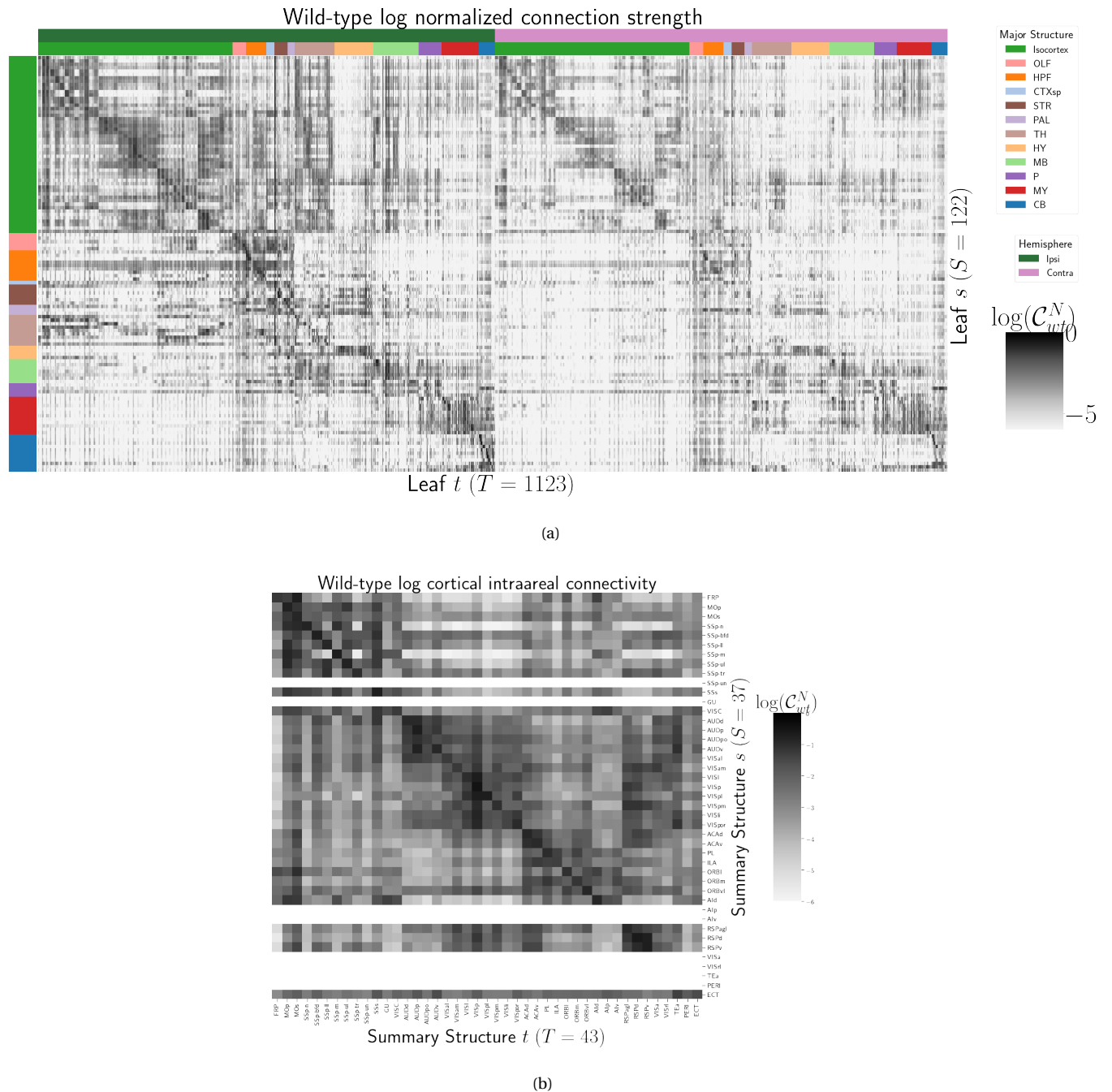


Figure 2: Wild-type connectivities. 2a Log wild-type connectivity matrix $\log \mathcal{C}(s, t, v_{wt})$. 2b Log wild-type intracortical connectivity matrix at the summary structure level.

243 *Class-specific connectivities* Since source and cell-type combinations which project similarly indicate
 244 the network structure underpinning cognition, we investigate the presence of several biological
 245 processes within our connectivity estimates. Although there is a rich anatomical literature using
 246 anterograde tracing data to describe projection patterns from subcortical sources to a small set of
 247 targets of interest, much of the accessible whole brain projection data is from the MCA project used
 248 here to generate the connectome models. Thus, to validate our results while avoiding a circular
 249 validation of the data used to generate the model weights, we confirm that these class-specific
 250 connectivities exhibit certain known behaviors. The cell types and source areas with extensive
 251 previous anatomical descriptions of projections using both bulk tracer methods with cell type
 252 specificity and single cell reconstructions that we investigate are 1) thalamic-projecting neurons in
 253 the visual and motor cortical regions, 2) cholinergic neurons in the medial septum and nucleus of the
 254 diagonal band (MS/NDB); and 3) serotonergic neurons of the dorsal raphe nucleus (DR). Our
 255 estimated connections are in agreement with literature on these cell types.

256 DEPENDENCE OF THALAMIC CONNECTION ON CORTICAL LAYER. Visual cortical areas VISp and VISl and
 257 cortical motor areas MOp and MOs have established layer-specific projection patterns that can be
 258 labeled with the layer-specific Cre-lines from the Allen datasets and others J. A. Harris et al. (2019);
 259 Jeong et al. (2016). Figure 3a shows that in VISp, the Ntsr1-Cre line strongly targets the core part of the
 260 thalamic LGd nucleus while in VISl, it a strong projection to the LP nucleus. In VISp, the Rbp4-Cre line
 261 strongly targets LP as well. Rbp4-Cre and Ntsr1-Cre injections target layers 5 and 6 respectively. Since
 262 we only generate connectivity estimates for structures with at least one injection centroid, this is
 263 shown by the position of non-zero rows in Figure 3a. To fill these gaps, as a heuristic alternative
 264 model, we also display an average connectivity matrix over all Cre-lines.

265 MS AND NDB PROJECTIONS IN THE CHAT-IRES-CRE-NEO MODEL. Cholinergic neurons in the MS and
 266 NDB are well-known to strongly innervate the hippocampus, olfactory bulb, piriform cortex,
 267 entorhinal cortex, and lateral hypothalamus (Watson, Paxinos, & Puelles, 2012; Zaborszky et al., 2015).
 268 In the Allen MCA, cholinergic neurons were labeled by injections into Chat-IRES-Cre-neo mice.
 269 Figure 3b checks the estimated connectome weights to targets in these major brain divisions from MS
 270 and NDB. We observed that all these expected divisions were represented above the 90th percentile of
 271 weights from these source structures.

272 We also compared our Chat-IRES-Cre connectome model data for MS and NDB with the targets
 273 identified by Li et al. (2018). This single cell whole brain mapping project using Chat-Cre mice fully
 274 reconstructed n=50 cells to reveal these same major targets and also naming additional targets from
 275 MS/NDB (Li et al., 2018). We identified 150 targets at the fine leaf structure level among the top decile
 276 of estimated weights. To directly compare our data across studies, we merged structures as needed to
 277 get to the same ontology level, and remove ipsilateral and contralateral information. After formatting
 278 our data, we found 51 targets in the top 10%; Li et al. reported 47 targets across the 50 cells. There was
 279 good consistency overall between the target sets; 35 targets were shared, 12 were unique to the single
 280 cell dataset, and 16 unique to our model data. We checked whether targets missing from our dataset
 281 were because of the threshold level. Indeed, lowering the threshold to the 75 th percentile confirmed 6
 282 more targets-in-common, and all but 2 targets from Li et al. (2018) were above the 50th percentile
 283 weights in our model. Of note, the absence of a target in the single cell dataset that was identified in
 284 our model data is most likely due to the sparse sampling of all possible projections from only n=50
 285 MS/NDB cells.

286 DR PROJECTIONS IN THE SLC6A4-CRE'ET33 MODEL. Serotonergic projections from cells in the
 287 dorsal raphe (DR) are widely distributed and innervate many forebrain structures including isocortex
 288 and amygdala. In the Allen MCA, serotonergic neurons were labeled using Slc6a4-Cre_ET33 and
 289 Slc6a4-CreERT2_EZ13 mice. This small nucleus appears to contain a complex mix of molecularly
 290 distinct serotonergic neuron subtypes with some hints of subtype-specific projection patterns (Huang
 291 et al., 2019; Ren et al., 2018, 2019). We expect that the Cre-lines used here in the Allen MCA, which use
 292 the serotonin transporter promoter (Slc6a4-Cre and -CreERT2), will lead to expression of tracer in all
 293 the serotonergic subtypes recently described in an unbiased way, but this assumption has not been
 294 tested directly. We compared our model data to a single cell reconstruction dataset consisting of n=50
 295 serotonergic cells with somas in the DR that also had bulk tracer validation 3c. After processing our
 296 data to match the target structure ontology level across studies, we identified 37 targets from the DR
 297 with weights above the 90th percentile, whereas Ren et al. (2019) listed 55 targets across the single cell
 298 reconstructions. Twenty seven of these targets where shared.

299 Overall there was good consistency between targets in olfactory areas, cortical subplate, CP, ACB
 300 and amygdala areas, as well in palidum and midbrain, while the two major brain divisions with the

301 least number of matches are the isocortex and thalamus. There are a few likely reasons for these
302 observations. First, in the isocortex, there is known to be significant variation in the density of
303 projections across different locations, with the strongest innervation in lateral and frontal orbital
304 cortices Ren et al. (2019); ?. Indeed, when we lower the threshold and check for weights of the targets
305 outside of the 90%, we see all but one of these regions (PTLp, parietal cortex which is not frontal or
306 lateral) has a weight assigned in the top half of all targets. In the thalamus, our model predicted strong
307 connections to several medial thalamic nuclei (i.e., MD, SMT) that were not targeted by the single
308 cells. This discrepancy may be at least partially explained by the complex topographical organization
309 of the DR that, like the molecular subtypes, is not yet completely understood. A previous bulk tracer
310 study that specifically targeted injections to the central, lateral wings, and dorsal subregions of the DR
311 reported semi-quantitative differences in projection patterns (Muzerelle, Scotto-Lomassese, Bernard,
312 Soiza-Reilly, & Gaspar, 2016). Notably, Muzerelle et al. (2016) report that cells in the ventral region of
313 DR project more strongly to medial thalamic nuclei, whereas the lateral and dorsal DR cells innervate
314 more lateral regions (e.g., LGd). Thus, it is possible that the single cell somas did not adequately
315 sample the entire DR.

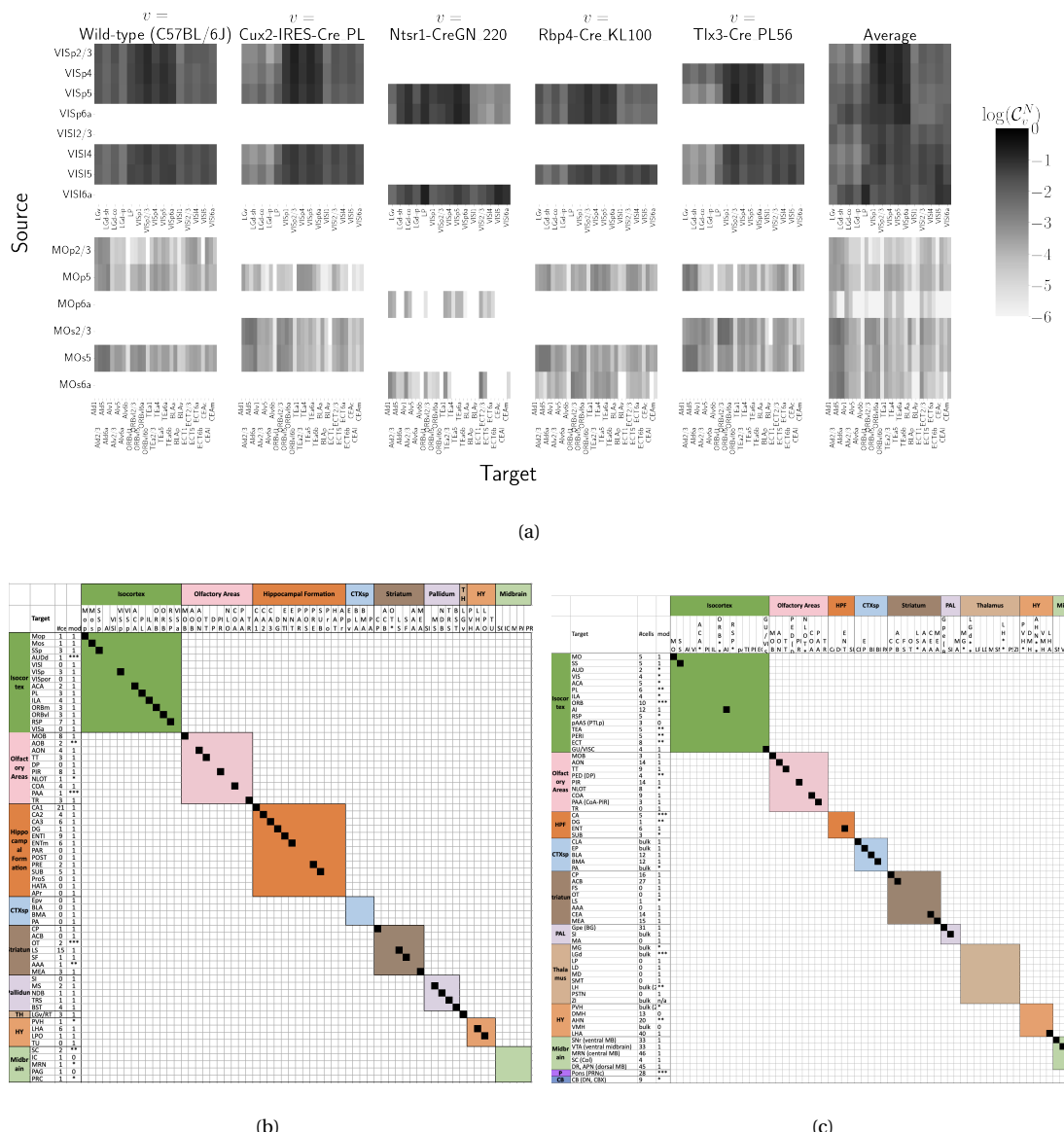


Figure 3: Cell-class specificity. 3a Selected cell-class and layer specific connectivities from two visual and two motor areas. Sources without an injection in the Cre driver line are not estimated due to lack of data for that Cre-line in that structure. 3b Targets reported for cholinergic cells in MS/NDB in Li et al. (2018) and above the 90th percentile in our Chat-IRES-Cre-neo model. A black box along the diagonal indicates the target was identified in both studies ($n = 35$). The number of single cells (out of 50) with a projection to each target is shown in the first column after the target acronym and the next column shows whether a target appeared in the 90% thresholded model weights (1= present, 0=absent). Some of these targets only appeared at lower thresholds as indicated by asterisks, * * * > 85th%, ** > 75th%, * > 50th%. 3c Targets reported for serotonergic cells in DR in Ren et al. (2018, 2019) and above the 90th percentile in our Slc6a4-Cre_ET33 model.

316 *Connectivity Analyses*

317 Cell-class, while often correlated with cortical layer, can be a stronger driver of connectivity than
318 summary structure especially when looking at targets at major brain division level. Figure ?? shows a
319 collection of connectivity strengths generated using cre-specific models for wild-type, Cux2, Ntsr1,
320 Rbp4, and Tlx3 cre-lines from VIS areas at leaf level in the cortex to cortical and thalamic nuclei. We
321 use hierarchical clustering to sort source structure/cell-class combinations by the similarity of their
322 structural projections, and sort target structures by the structures from which they receive
323 projections. Examining the former, we can see that the layer 6 Ntsr1 Cre-line distinctly projects to
324 thalamic nuclei, regardless of source summary structure. This contrasts with the tendency of other
325 cell-classes to project intracortically in a manner determined by the source structure. Similarly, layer 6
326 targets are not strongly projected to by any of the displayed cell classes.

327 This exploratory analysis lead us to investigate matrix decomposition methods for our estimated
328 connectivity matrices. We applied non-negative matrix factorization to decompose the long-range
329 wild-type connectivities into linear combinations of learned latent connectivities. In particular, we
330 censor short range connections due to their clear biological derivation from diffusion and their high
331 mathematical rank. This decomposes the remaining censored connectivity matrix into a linear model
332 based off a relatively small number of distinct signals.

333 In contrast to the complex tree of cell types implied by heirarchical clustering, this creates a simple
334 linear statistical model of overall connectivity. These signals are plotted in Figure 4, and technical
335 details and intermediate results are given in Supplemental Sections 6 and 7, respectively. The matrix
336 factorization model captures a large amount of the observed variability, both in the statistical sense,
337 and also in terms of its ability to generate a reconstructed connectivity matrix with structure and
338 layer-specific targeting from a relatively small number of learned additive factors. Since underlying
339 tissues are heterogenous, it is plausible that these factors reflect a mixture of cell-types. Thus, we
340 associate the factors in this model with individual Cre-lines, and find that certain factors correspond
341 to several of our Cre-lines.

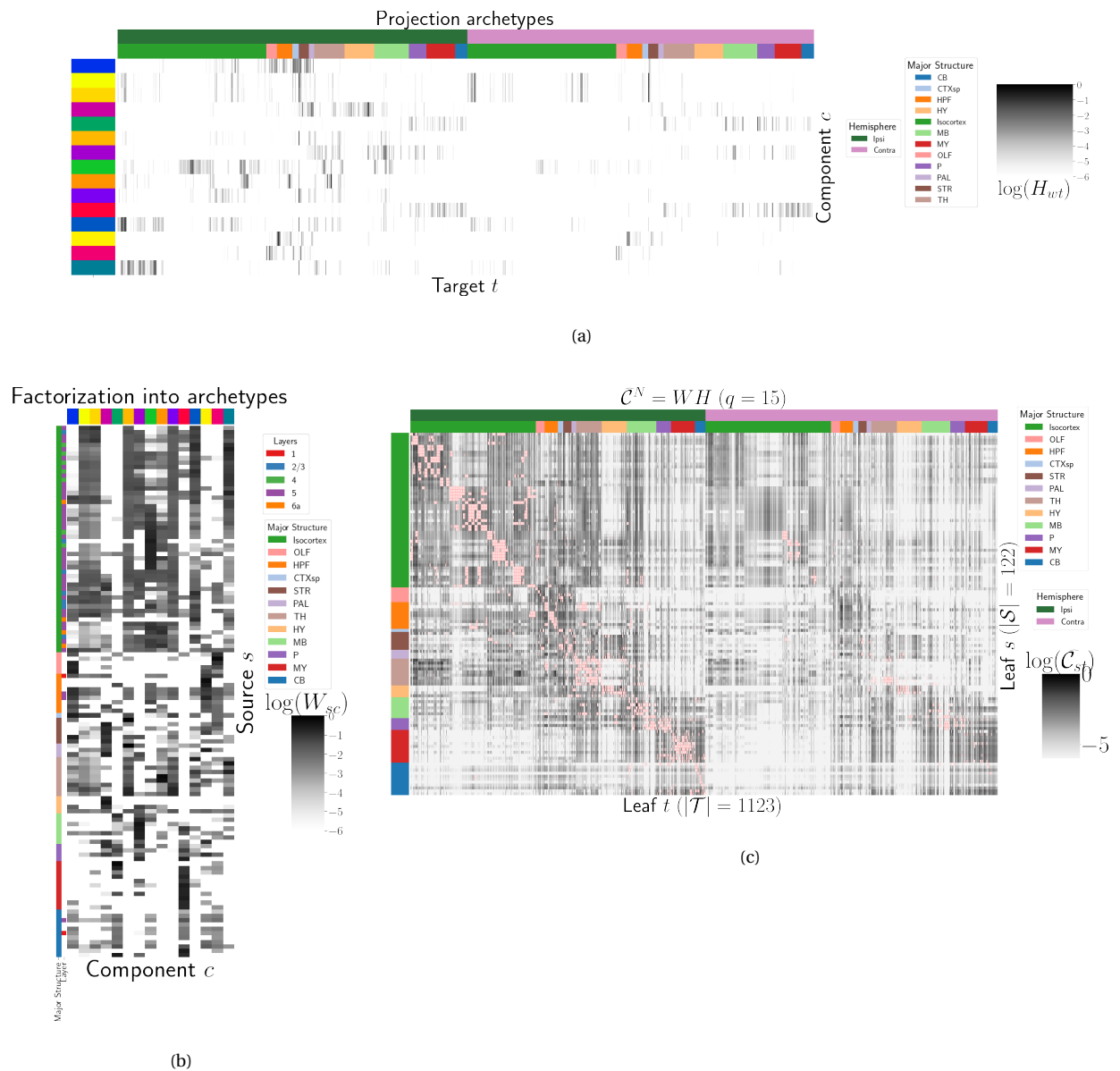


Figure 4: Non-negative matrix factorization results $\mathcal{C}_w^N = W H$ for $q = 15$ components. 4a Latent space coordinates H of \mathcal{C} . Target major structure and hemisphere are plotted. 4b Loading matrix W . Source major structure and layer are plotted. 4c Reconstruction of the normalized distal connectivity strength using the top 15 archetypes. Areas less than $1500\mu m$ apart are not modeled, and therefore shown in red.

4 DISCUSSION

342 The model presented here is the first cell-type specific whole brain projectome model for a
 343 mammalian species, and it opens the door for a large number of models linking brain structure to
 344 computational architectures. Overall, we find expected targets, based on our anatomical expertise
 345 and published reports, but underscore that the core utility of this bulk connectivity analysis is not
 346 only in validation of existing connection patterns, but also in identification of new ones. We note that
 347 although the concordance appeared stronger for the cholinergic cells than the serotonergic cells, any
 348 differences might still be explained by the lack of high quality “ground-truth” datasets to validate
 349 these Cre connectome models. Larger numbers of single cell reconstructions, that saturate all
 350 possible projection types, would be a better gold standard than the small number of cells reported
 351 here (n=50 for each). ([SK's comment: add citation](#)) Perhaps future iterations of the connectome model
 352 may also take into account some single cell axon projection data.

353 The Nadaraya-Watson estimator presented here is novel. Beyond using a Nadaraya-Watson kernel
 354 regression defined in physical space, we define a cell-type space based on similarities of projections,
 355 and theoretically justify the use of an intermediate shape-constrained estimator. While methods like
 356 non-negative least squares can also account for covariates, the centroid method from Knox et al.
 357 (2019) was shown that the more precise notion of injection location than the non-negative least
 358 squares in Oh et al. (2014). Furthermore, our sample size seems too low to utilize a fixed or mixed
 359 effect, particularly since the impact of the virus depend on the particular injection region. In a sense
 360 both the NNLS and NW models can be thought of as improvements over the structure-specific
 361 average, and so is also possible that a yet undeveloped residual-based data-driven blend of these
 362 models could provide improved performance.

363 We see several other opportunities for improving on our model. Ours is certainly not the first
 364 cross-validation based model averaging method Gao, Zhang, Wang, and Zou (2016). However, our use
 365 of shape-constrained estimator in target-encoded feature space is novel and fundamentally different
 366 from Nadaraya-Watson estimators that use an optimization method for selecting the weights (Saul &
 367 Roweis, 2003). The properties of this estimator, as well as its relation to estimators fit using an
 368 optimization algorithm, are a possible future avenue of research. A deep model such as Lotfollahi,
 369 Naghipourfar, Theis, and Alexander Wolf (2019) could be appropriate, provided enough data was

370 available. Finally, a Wasserstein-based measure of injection similarity per structure would combine
371 both the physical simplicity of the centroid model while also incorporating the full distribution of the
372 injection signal.

373 The factorization of the connectivity matrix could also be improved and better used. From a
374 statistical perspective, stability-based method for establishing archetypal connectivities in NMF is
375 similar to those applied to genomic data Kotliar et al. (2019); Wu et al. (2016). However, non-linear
376 data transformations or matrix decompositions, or tensor factorizations that account for correlations
377 between cell-types could better capture the true nature of archetypal neural connections. It would
378 also be of great interest to associate the archetypal signals detected from connectivity analysis with
379 undergirding gene expression patterns or functional information.

380 Inspired by how this complexity arises from a relatively parsimonious set of genetic information
381 during development, w Such components can provide a link to the genetic origin of the regionalized
382 connectivity.

ACKNOWLEDGMENTS

³⁸³ We thank the Allen Institute for Brain Science founder, Paul G. Allen, for his vision, encouragement,
³⁸⁴ and support.

385 This supplement is divided into information about our dataset, supplemental methods, and
386 supplemental results. However, certain topics are revisited between sections. Thus, if a reader is
387 interested in, say, non-negative matrix factorization, they may find relevant information in both
388 methods and results.

5 SUPPLEMENTAL INFORMATION

389 Our supplementary information consists of abundances of leaf/Cre-line combinations, information
390 about distances between structures, and the size of our restricted evaluation dataset.

391 *Cre/structure combinations in \mathcal{D}*

392 This section describes the abundances of leaf and Cre-line combinations in our dataset. Users of the
393 connectivity matrices who are interested in a particular Cre-line or structure can see the quantity and
394 type of data used to compute and evaluate that connectivity.

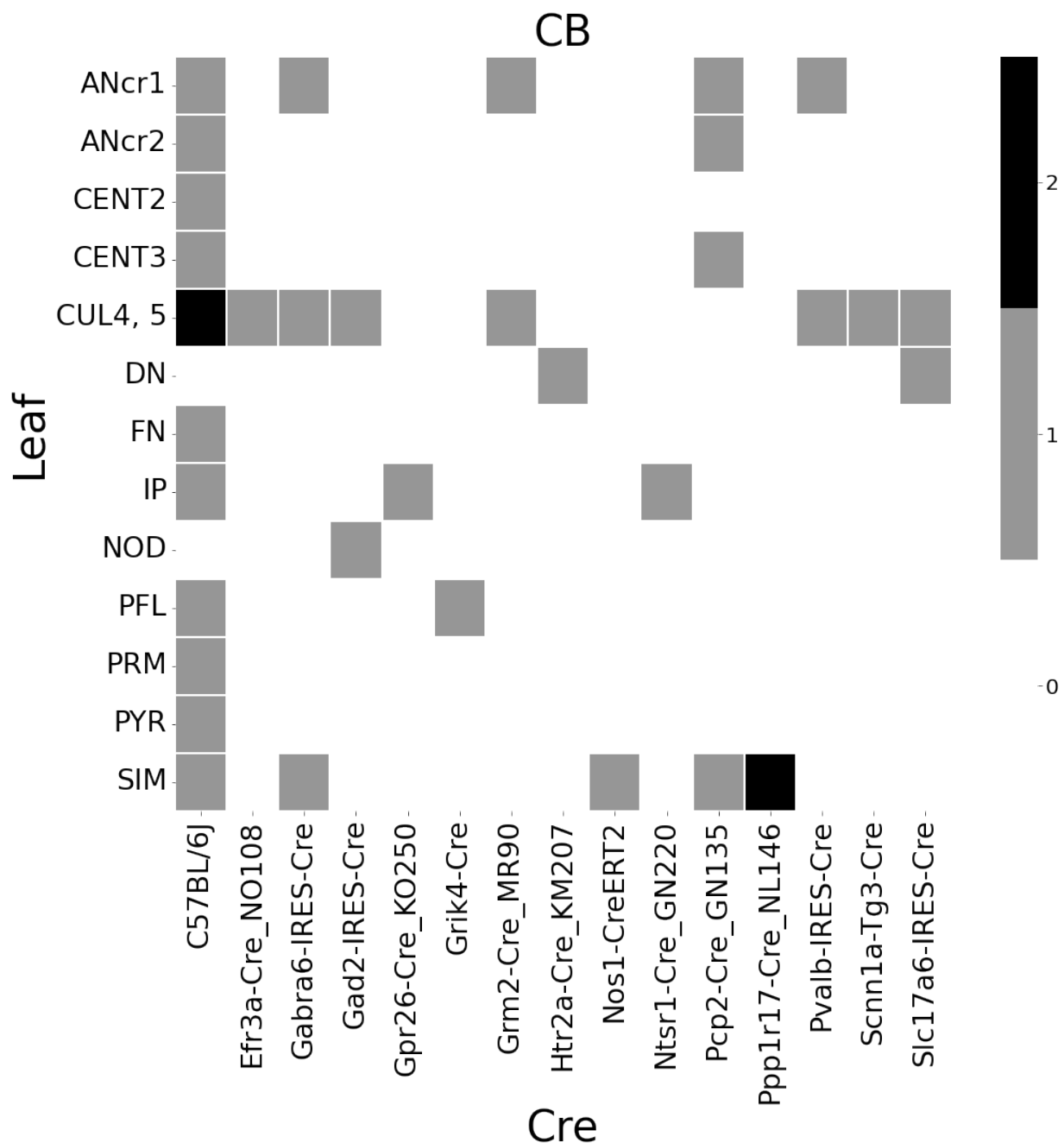


Figure 5: Abundances of Cre-line and leaf-centroid combinations.

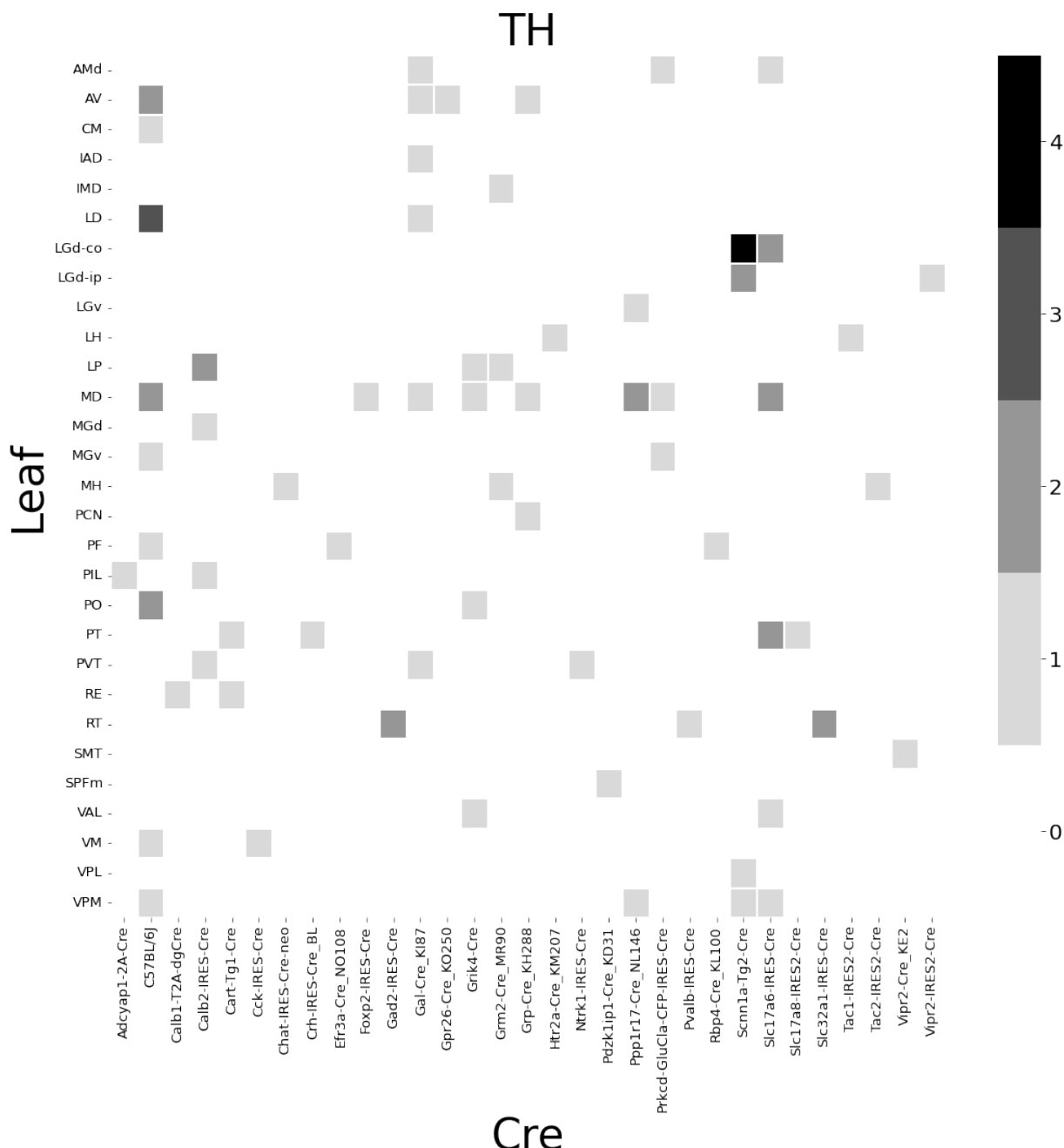


Figure 6: Abundances of Cre-line and leaf-centroid combinations.

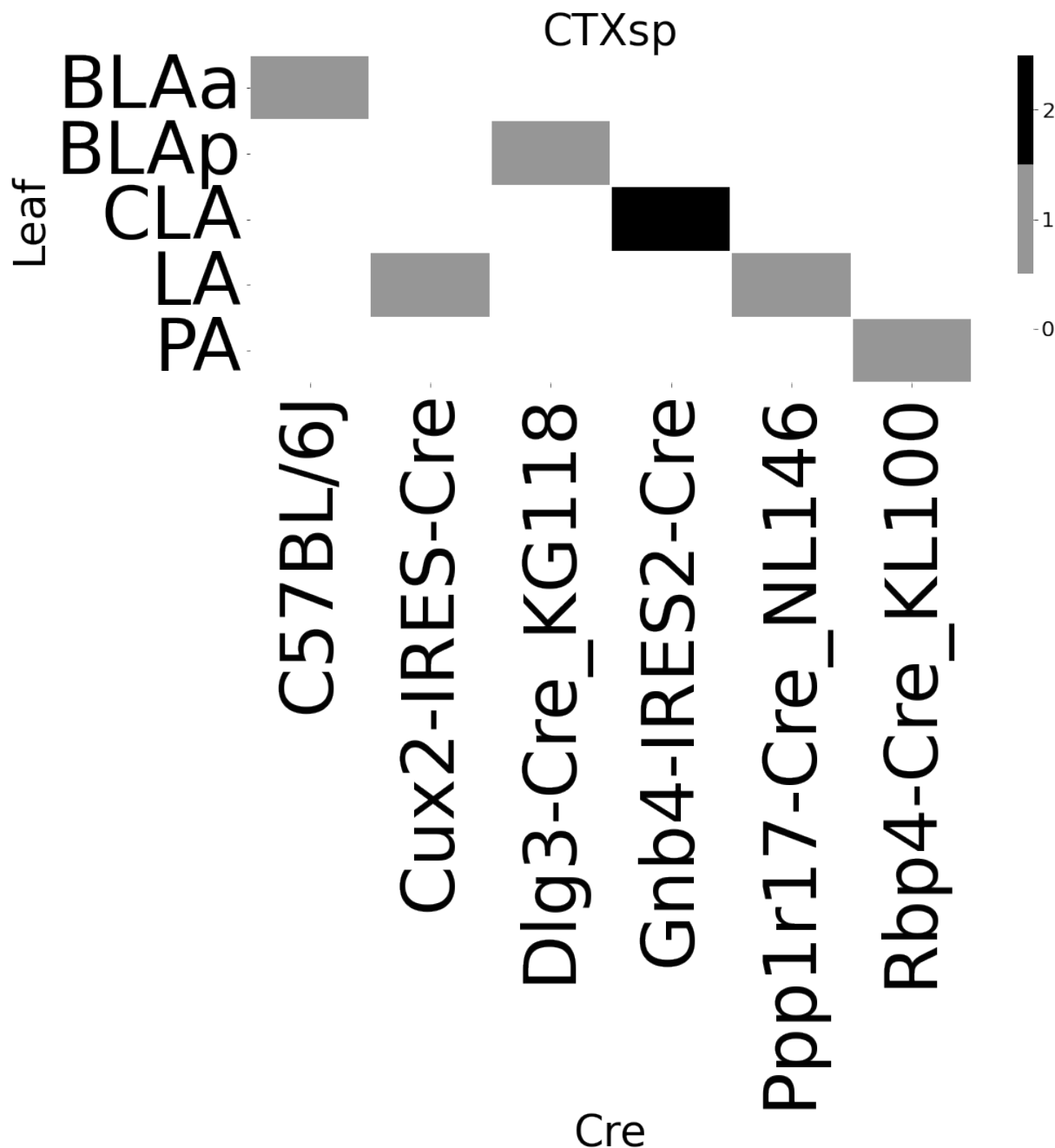


Figure 7: Abundances of Cre-line and leaf-centroid combinations.

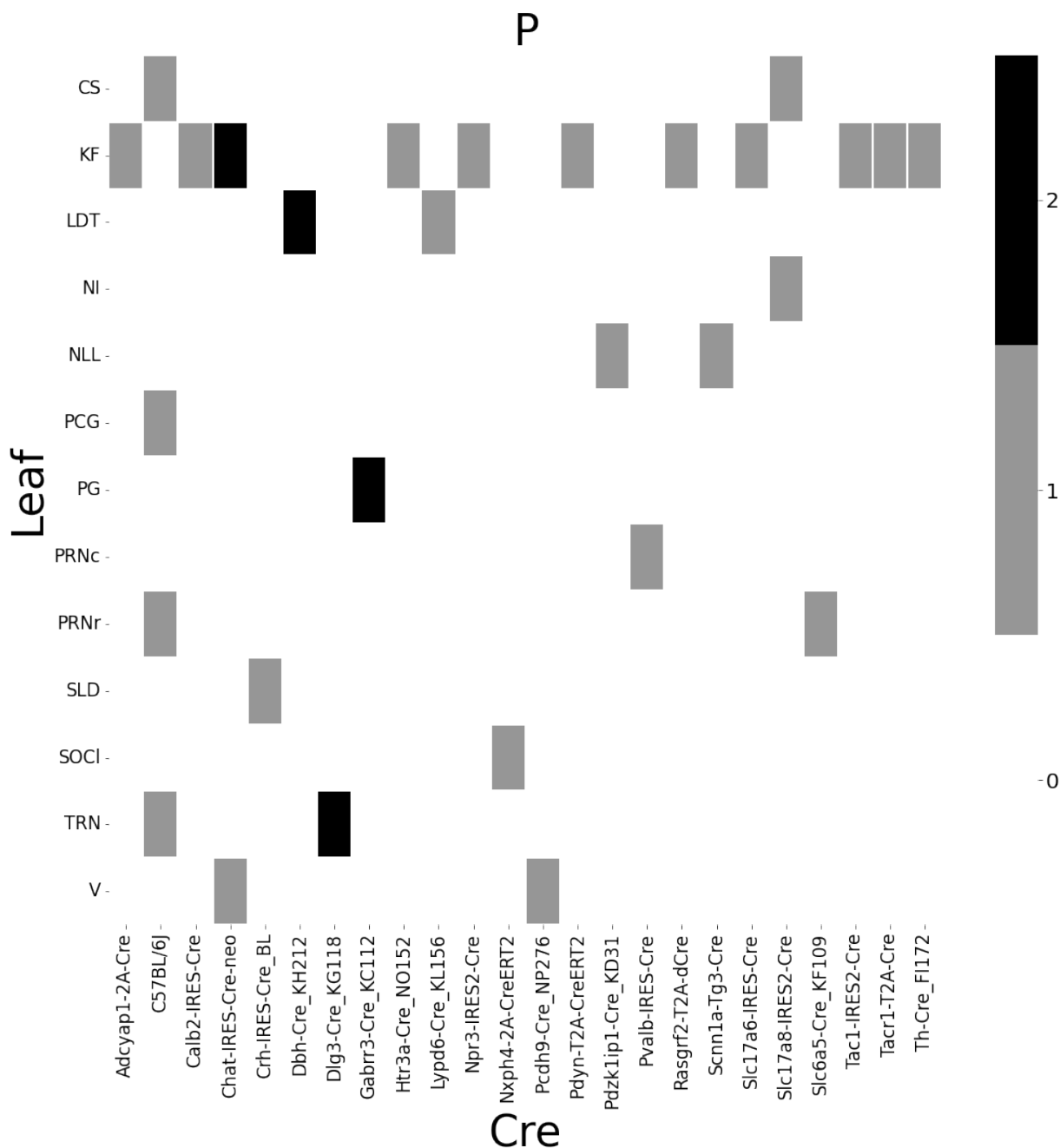


Figure 8: Abundances of cre-line and leaf-centroid combinations.

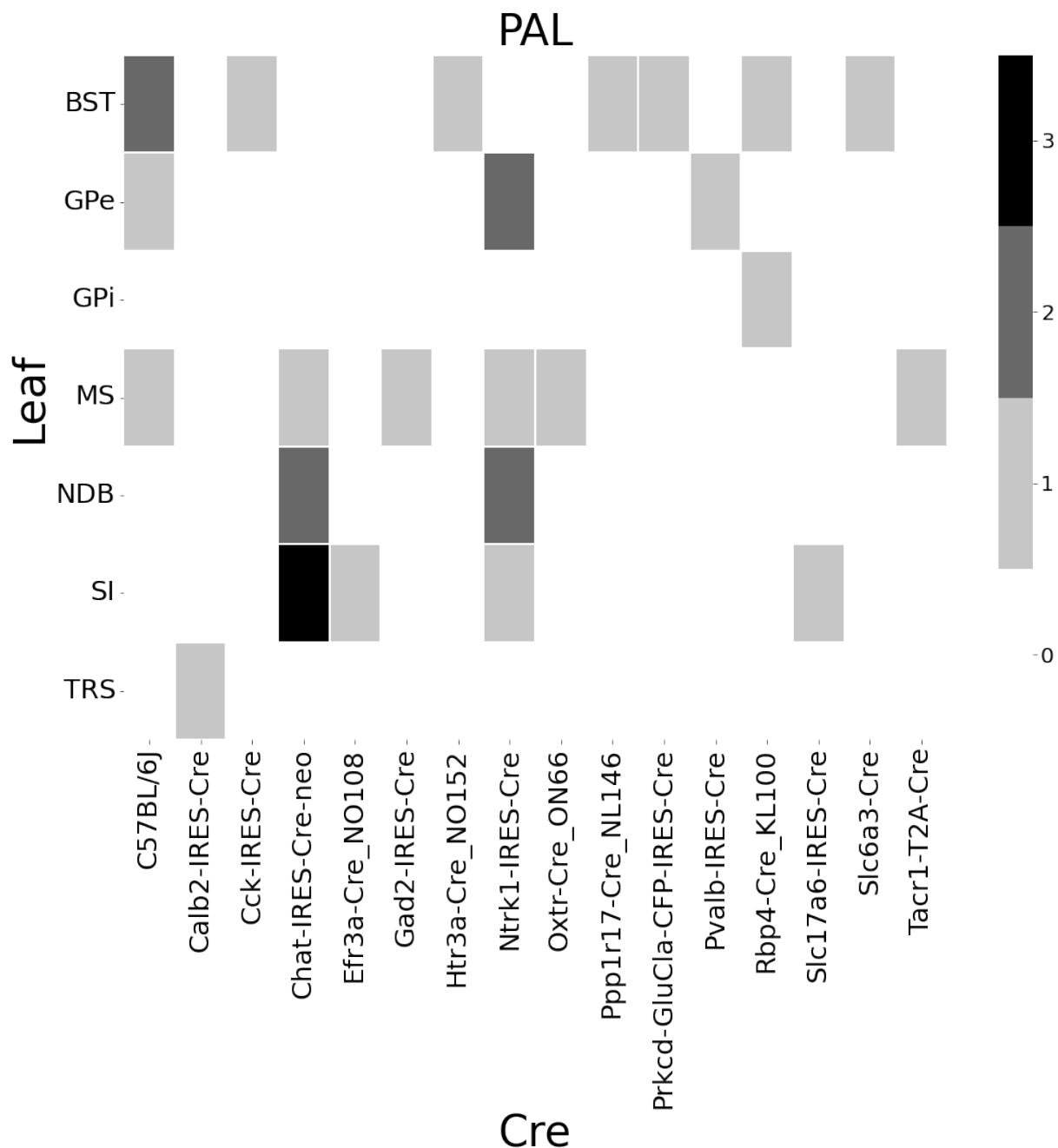


Figure 9: Abundances of Cre-line and leaf-centroid combinations.

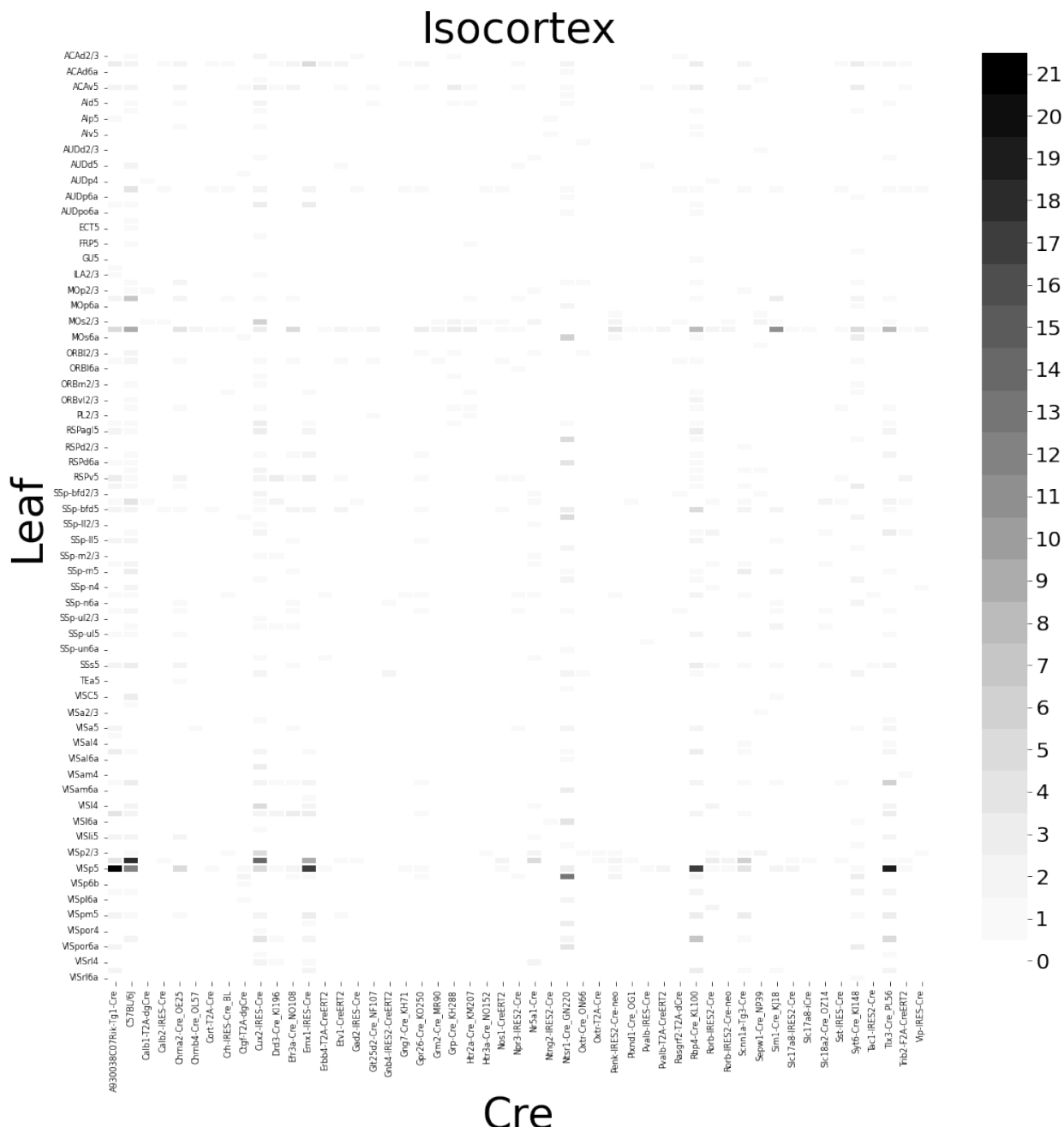


Figure 10: Abundances of Cre-line and leaf-centroid combinations.

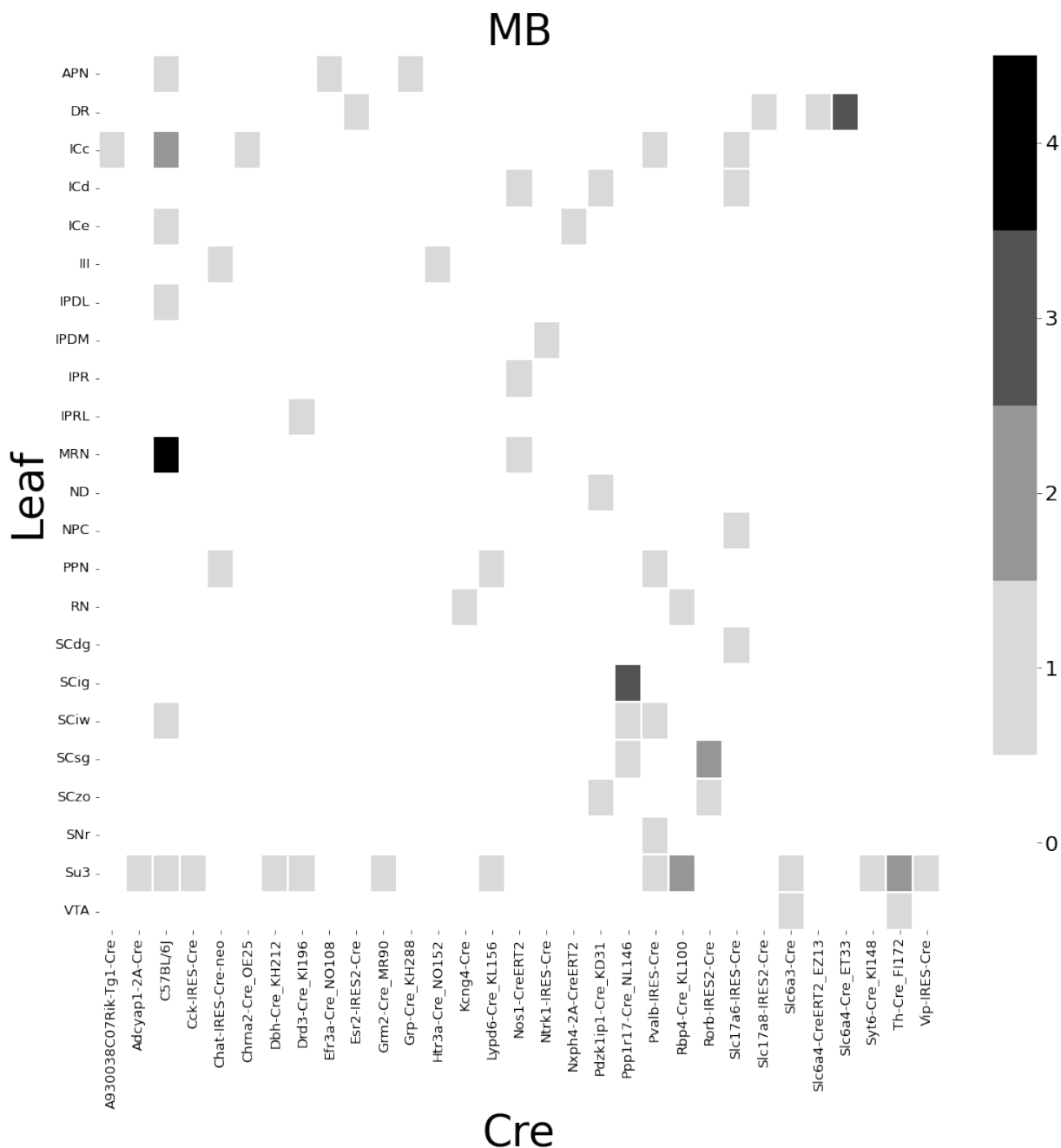


Figure 11: Abundances of Cre-line and leaf-centroid combinations.

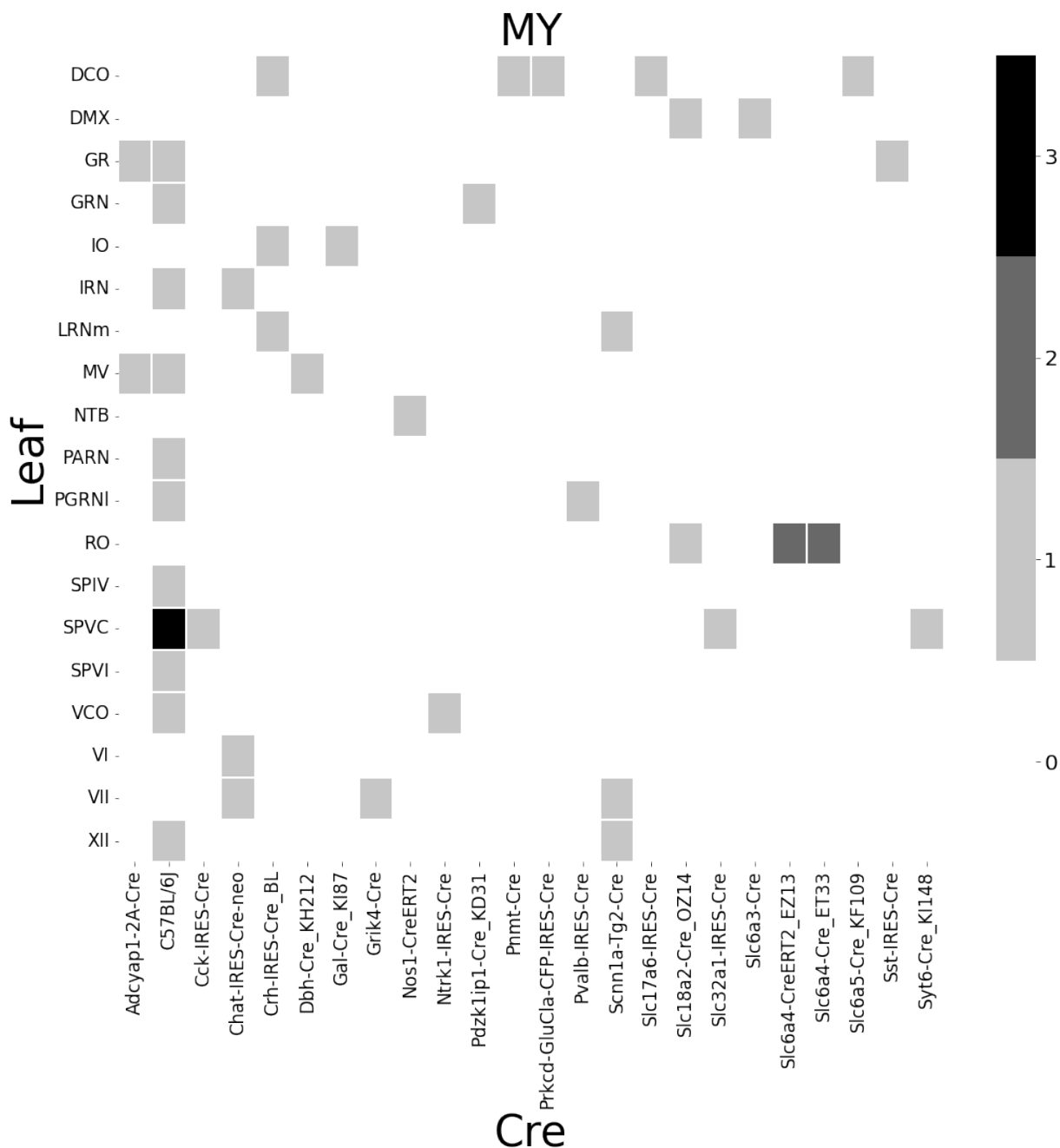
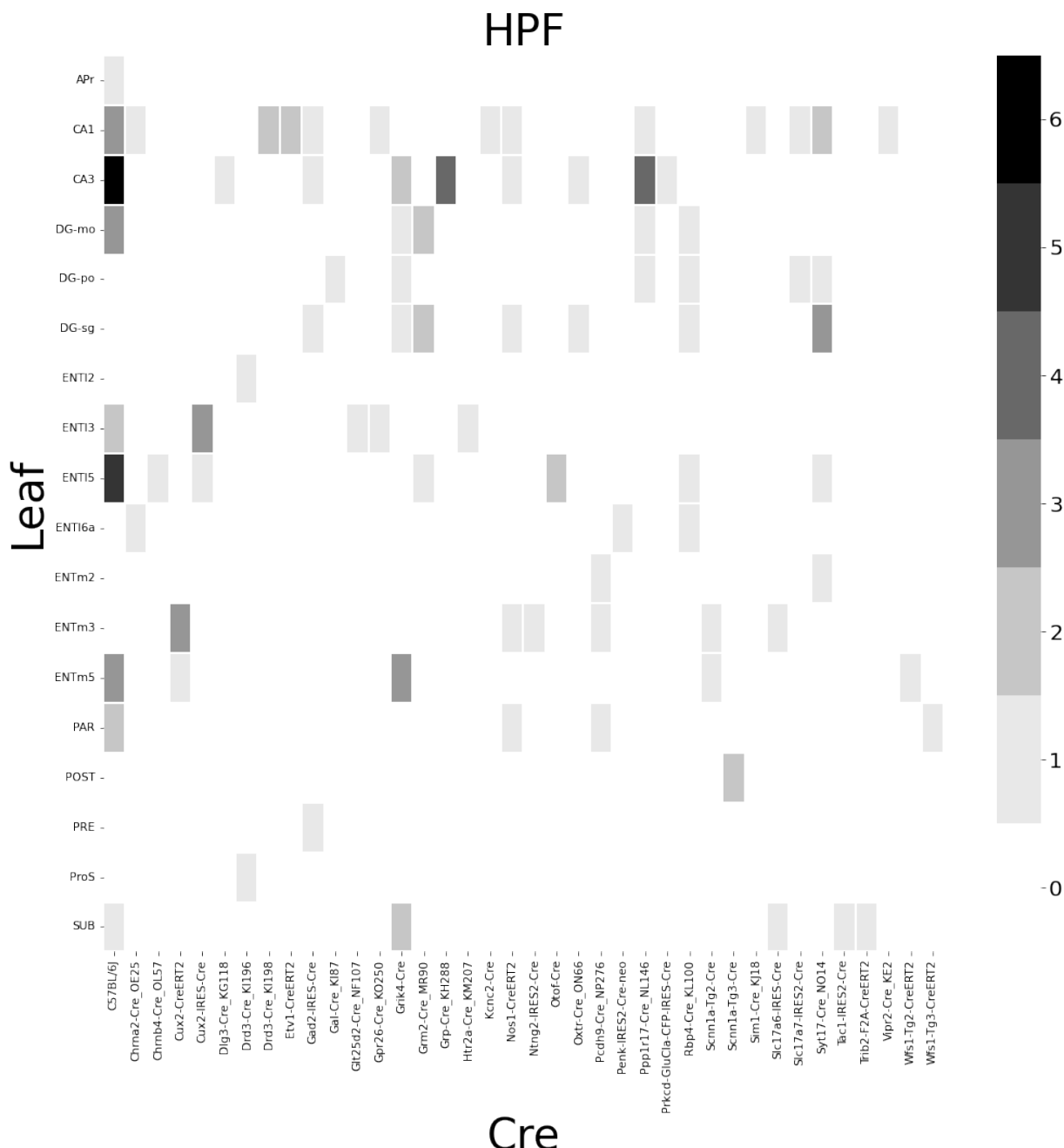


Figure 12: Abundances of Cre-line and leaf-centroid combinations.



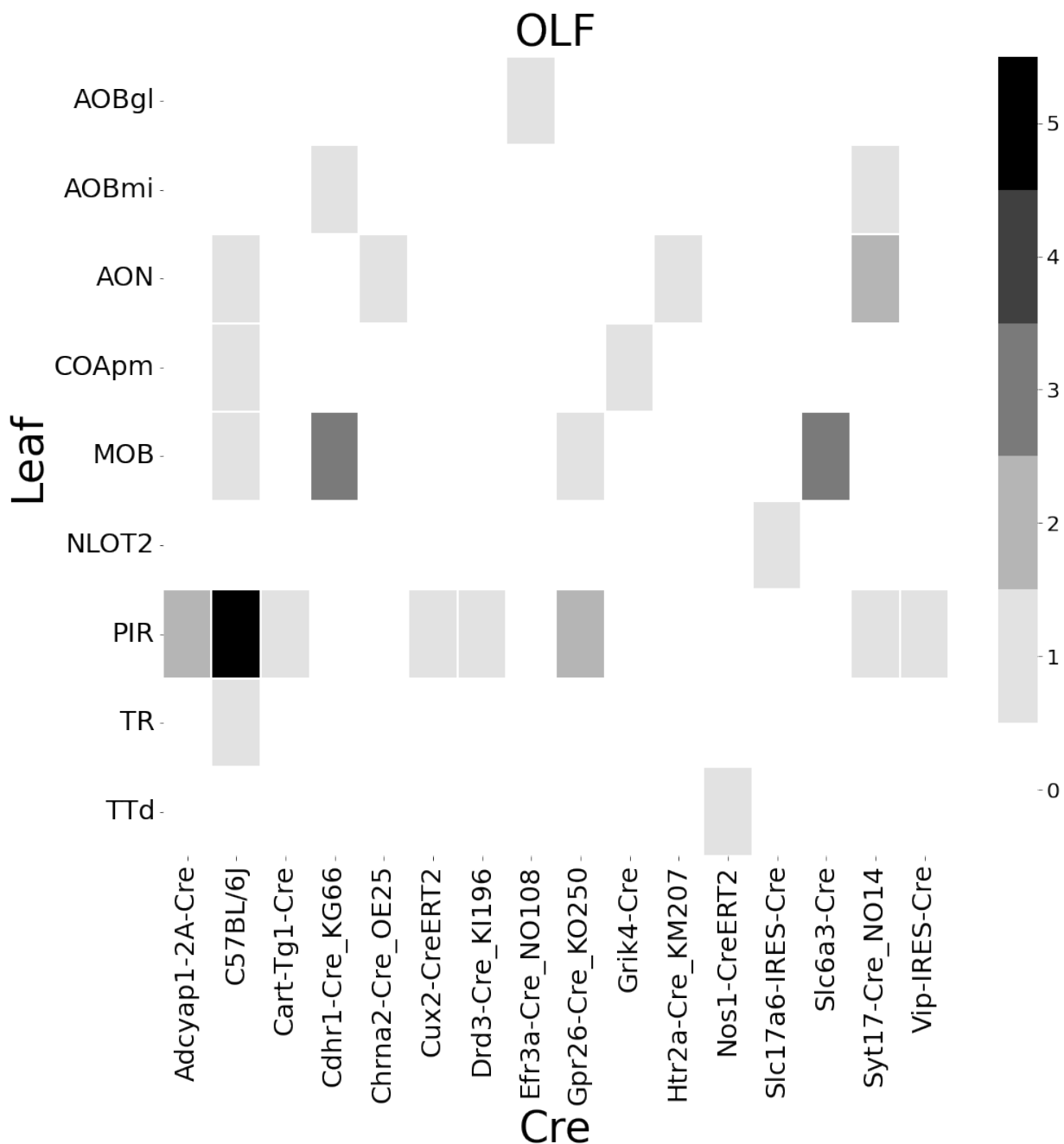


Figure 14: Abundances of Cre-line and leaf-centroid combinations.

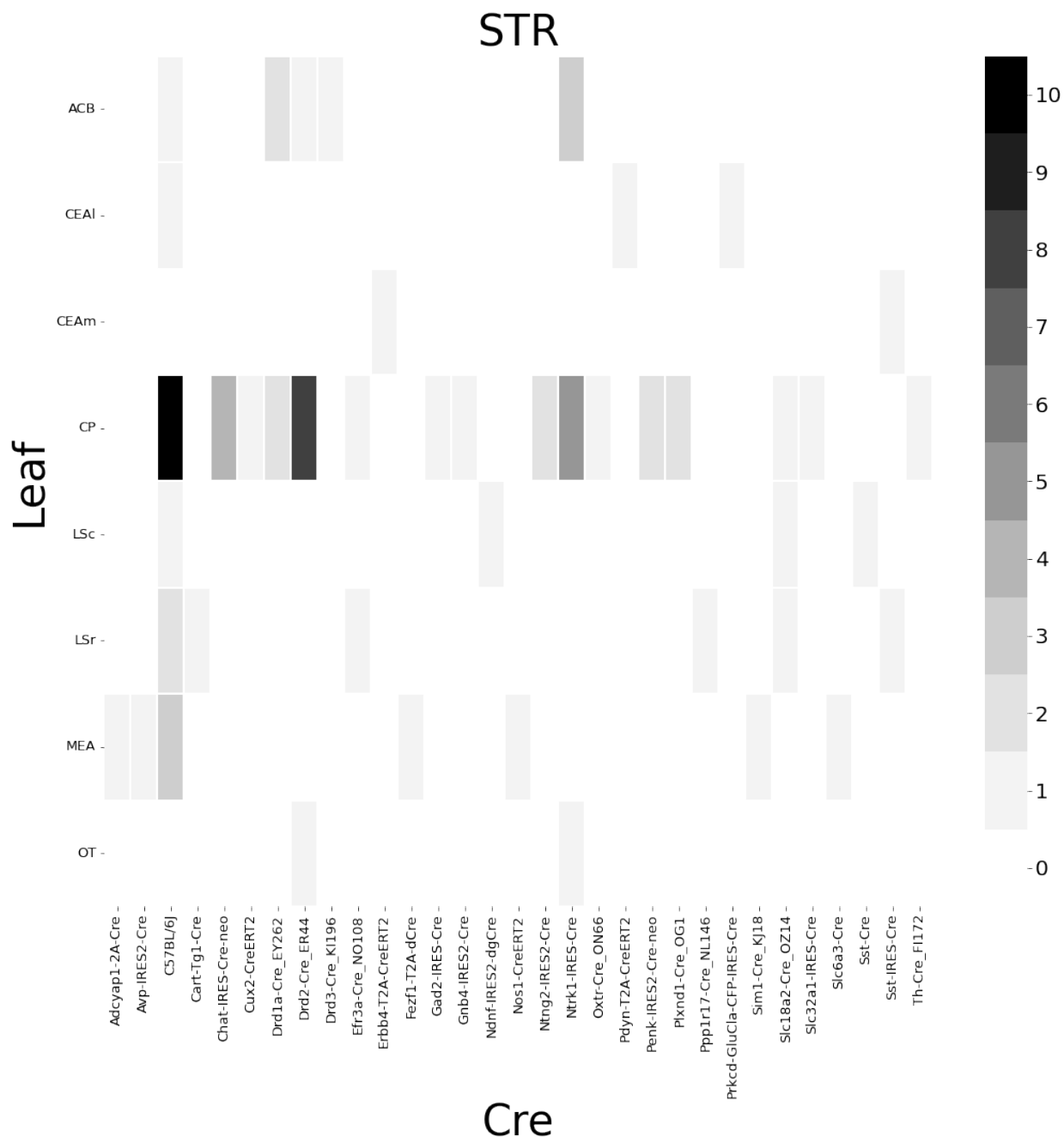


Figure 15: Abundances of Cre-line and leaf-centroid combinations.

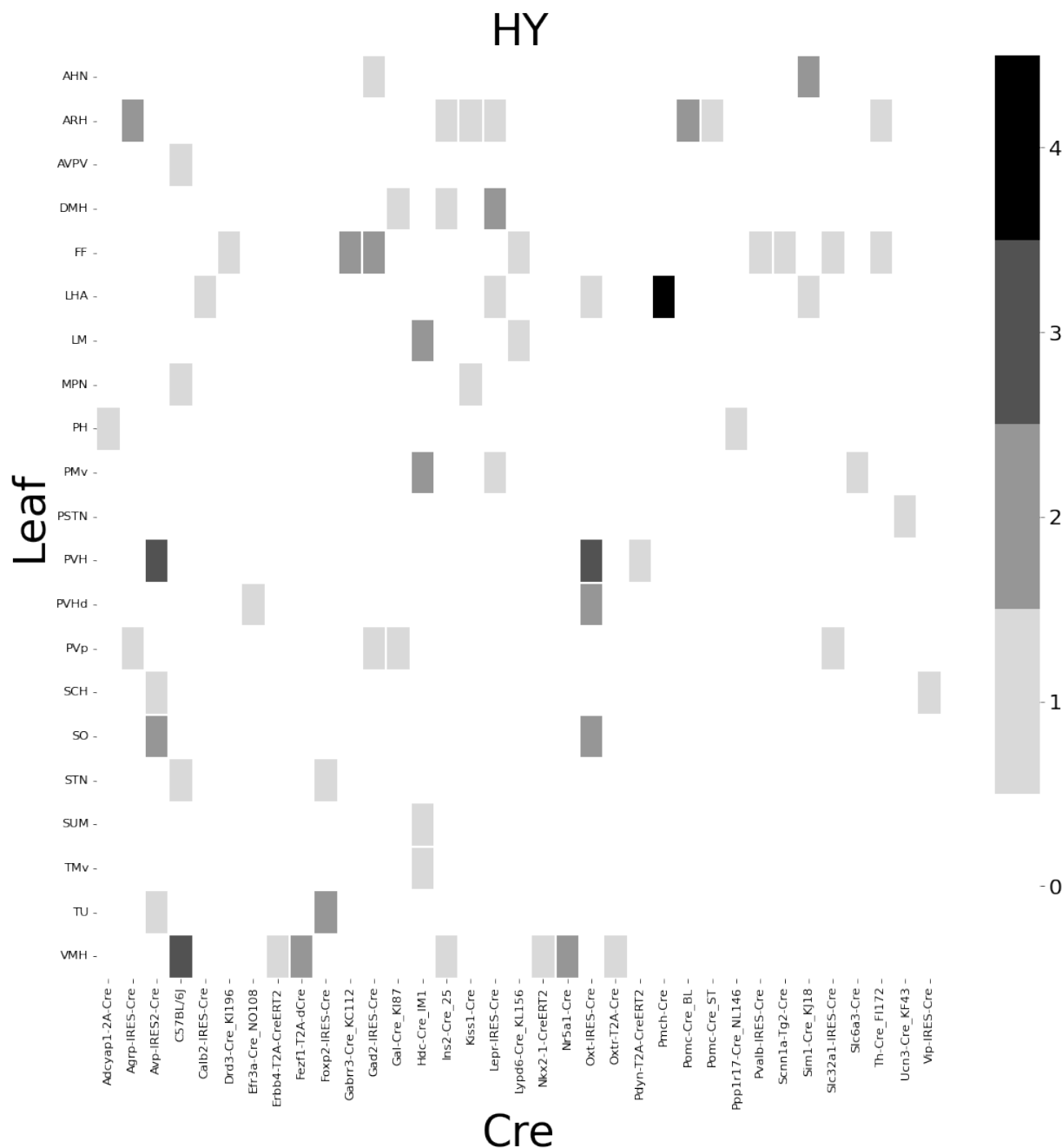


Figure 16: Abundances of Cre-line and leaf-centroid combinations.

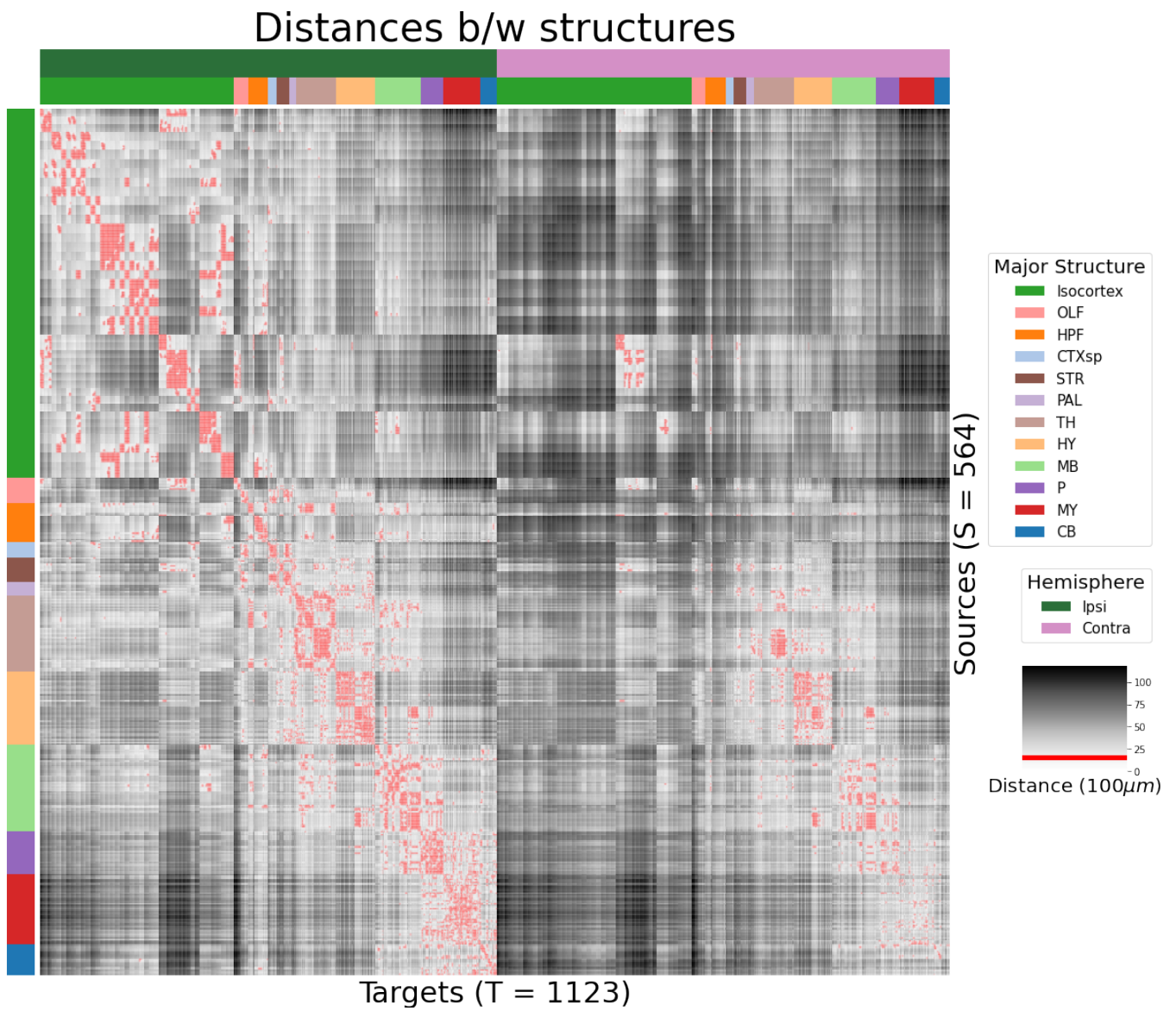
395 ***Distances between structures***

Figure 17: Distance between structures. Short-range connections are masked in red

396 ***Model evaluation***

397 We give information on the quality of our models. This includes the sizes of our evaluation sets in
 398 leave-one-out cross-validation and additional losses in the injection-normalized case.

399 NUMBER OF EXPERIMENTS IN EVALUATION SETS In order to compare between methods, we therefore
 400 restrict to the smallest set of evaluation indices, which is to say, virus-leaf combinations that are
 401 present at least twice. This means that our evaluation set is smaller in size than our overall list of
 402 experiments.

	Total	Cre-Leaf	Cre-leaf over threshold
Isocortex	36	4	4
OLF	7	2	2
HPF	122	62	59
CTXsp	85	41	38
STR	1128	732	7
PAL	68	18	17
TH	46	7	7
HY	35	17	17
MB	33	8	8
P	30	11	11
MY	78	45	44
CB	83	29	29

Table 3: Number of experiments available to evaluate models in leave-one-out cross validation. Models that rely on a finer granularity of modeling have less data available to validate with.

403 INJECTION-NORMALIZED LOSSES To compare with the injection-normalization procedure from Knox
 404 et al. (2019), we also remove experiments with small injection, and here give results for this slightly
 405 reduced set using injection-normalization. That is, instead of dividing the projection signal of each
 406 experiment by its l_1 norm, we divide by the l_1 norm of the corresponding injection signal. We find
 407 that setting a summed injection-signal of threshold of 1 is sufficient for evading pathological edge
 408 cases in this normalization, while still retaining a large evaluation set.

\hat{f}	Mean	NW					EL
\mathcal{D}	$I_c \cap I_L$	$I_c \cap I_M$	$I_c \cap I_L$	I_L	$I_{wt} \cap I_M$	I_M	I_L
Isocortex	0.413	0.453	0.408	0.538	0.528	0.528	0.396
OLF	0.499	0.504	0.494	0.441	0.543	0.543	0.437
HPF	0.336	0.483	0.332	0.444	0.501	0.501	0.321
CTXsp	0.497	0.497	0.497	0.497	0.497	0.497	0.497
STR	0.359	0.386	0.359	0.364	0.433	0.433	0.322
PAL	0.519	0.497	0.519	0.436	0.459	0.459	0.434
TH	0.769	0.767	0.769	0.514	0.539	0.539	0.556
HY	0.414	0.439	0.414	0.441	0.452	0.452	0.399
MB	0.459	0.396	0.397	0.358	0.324	0.324	0.403
P	0.562	0.562	0.562	0.758	0.764	0.764	0.562
MY	0.699	0.552	0.621	0.439	0.578	0.578	0.439
CB	0.849	0.689	0.849	0.500	0.615	0.615	0.495

Table 4: Losses from leave-one-out cross-validation of candidate for injection-normalized regionalized connectivity on injection-thresholded evaluation set. **Bold** numbers are best for their major structure.

409 PROJECTION-NORMALIZED LOSSES ON THRESHOLDED SET We also give results for the
 410 projection-normalization procedure from the main text on this reduced subset.

\hat{f}	Mean	NW	EL				
\mathcal{D}	$I_c \cap I_L$	$I_c \cap I_M$	$I_c \cap I_L$	I_L	$I_{wt} \cap I_M$	I_M	I_L
Isocortex	0.229	0.248	0.224	0.274	0.269	0.269	0.217
OLF	0.193	0.233	0.191	0.135	0.179	0.179	0.138
HPF	0.178	0.342	0.172	0.212	0.235	0.235	0.172
CTXsp	0.621	0.621	0.621	0.621	0.621	0.621	0.621
STR	0.128	0.117	0.124	0.171	0.234	0.234	0.125
PAL	0.203	0.205	0.203	0.295	0.291	0.291	0.188
TH	0.673	0.664	0.673	0.358	0.379	0.379	0.417
HY	0.358	0.378	0.351	0.331	0.312	0.312	0.314
MB	0.168	0.191	0.160	0.199	0.202	0.202	0.160
P	0.292	0.292	0.292	0.299	0.299	0.299	0.287
MY	0.268	0.347	0.268	0.167	0.189	0.189	0.196
CB	0.062	0.062	0.062	0.068	0.108	0.108	0.061

Table 5: Losses from leave-one-out cross-validation of candidate for normalized regionalized connectivity on injection-thresholded evaluation set. **Bold** numbers are best for their major structure.

6 SUPPLEMENTAL METHODS

⁴¹¹ This section consists of additional information on preprocessing of the neural connectivity data,
⁴¹² estimation of connectivity, and matrix factorization.

⁴¹³ ***Data preprocessing***

⁴¹⁴ Several data preprocessing steps take place prior to evaluations of the connectivity matrices. These
⁴¹⁵ steps are described in Algorithm PREPROCESS. The arguments of this normalization process - injection
⁴¹⁶ signals $x(i)$, projection signals $y(i)$, injection fraction $F(i)$, and data quality mask $q(i)$ - were
⁴¹⁷ downloaded using the Allen SDK. The injections and projection signals $\mathcal{B} \rightarrow [0, 1]$ were segmented
⁴¹⁸ manually in histological analysis. The projection signal gives the proportion of pixels within the voxel
⁴¹⁹ displaying fluorescence, and the injection signal gives the proportion of pixels within the
⁴²⁰ histologically-selected injection subset displaying fluorescence. The injection fraction $\mathcal{B} \rightarrow [0, 1]$ gives
⁴²¹ the proportion of pixels within each voxel in the injection subset. Finally, the data quality mask
⁴²² $\mathcal{B} \rightarrow \{0, 1\}$ gives the voxels that have valid data.

⁴²³ Our preprocessing makes use of the above ingredients, as well as several other essential steps. First,
⁴²⁴ we compute the weighted injection centroid

$$c(i) = \sum_{l \in \mathcal{B}} x(l) l$$

⁴²⁵ where $x(i)(l)$ is the injection density at location $l \in \mathbb{R}^3$. Given a regionalization \mathcal{R} from the Allen SDK,
⁴²⁶ we can also access regionalization map $R: \mathcal{B} \rightarrow \mathcal{R}$. This induces a functional of connectivities from
⁴²⁷ the space of maps $\{\mathcal{X} = x: \mathcal{B} \rightarrow [0, 1]$

$$\begin{aligned} 1_{\mathcal{R}}: \mathcal{X} &\rightarrow \mathcal{R} \times \mathbb{R}_{\geq 0} \\ x &\mapsto \sum_{l \in r} x(l) \text{ for } r \in \mathcal{R}. \end{aligned}$$

⁴²⁸ We also can restrict a signal to a individual structure as

$$\begin{aligned} 1|_s: \mathcal{X} &\rightarrow \mathcal{X} \\ x(l) &= \begin{cases} x(l) & \text{if } l \in S \\ 0 & \text{otherwise.} \end{cases} \end{aligned}$$

⁴²⁹ Finally, given a vector or array $a \in \mathbb{R}^T$, we have the $l1$ normalization map

$$n: a \mapsto \frac{a}{\sum_{j=1}^T a_j}.$$

⁴³⁰ We define these objects as functions and functionals, but this is for notational convenience and

⁴³¹ non-essential. A function $x(i) : \mathcal{B} \rightarrow [0, 1]$ is mathematically equivalent to the graph

⁴³² $\mathcal{G}(x(i)) \in \mathcal{B} \times [0, 1]$. As an abuse of notation, we define $x \odot x' := z$ such that $z(l) = x(l)x'(l)$ for all $l \in \mathcal{B}$.

⁴³³ Also, denote $m(i)$ as the major structure containing experiment i . We then can write the

⁴³⁴ preprocessing algorithm.

PREPROCESS 1 Input Injection x , Projection y , Injection centroid $c \in \mathbb{R}^3$, Injection fraction F , data quality mask q

Injection fraction $x_F \leftarrow x \odot F$

Data-quality censor $y_q \leftarrow y \odot q$, $x_q \leftarrow x_F \odot q$

Restrict injection $x_m = 1|_m x_q$.

Compute centroid c from x_m

Regionalize $\tilde{y}_{\mathcal{T}} \leftarrow 1_{\mathcal{T}}(y_q)$

Normalize $y_{\mathcal{T}} \leftarrow n(\tilde{y}_{\mathcal{T}})$

Output $\tilde{y}_{\mathcal{T}}, c$

435 **Estimators**

436 As mentioned previously, we can consider our estimators as modeling a connectivity vector
 437 $f_{\mathcal{T}}(\nu, s) \in \mathbb{R}_{\geq 0}^T$. Thus, for the remainder of this section, we will discuss only $f(\nu, s)$. We review the
 438 Nadaraya-Watson estimator from Knox et al. (2019), and describe its conversion into our cell-class
 439 specific Expected Loss estimator.

440 *Centroid-based Nadaraya-Watson* In the Nadaraya-Watson approach of Knox et al. (2019), the injection
 441 is considered only through its centroid $c(i)$, and the projection is considered regionalized. That is,

$$f_*(i) = \{c(i), y_{\mathcal{T}}(i)\}.$$

442 Since the injection is considered only by its centroid, this model only generates predictions for
 443 particular locations l , and the prediction for a structure s is given by integrating over locations within
 444 the structure

$$f^*(\hat{f}(f_*(\mathcal{D})))(\nu, s) = \sum_{l \in s} \hat{f}(f_*(\mathcal{D}(I)))(\nu, l).$$

445 Here, I is the training data, and \hat{f} is the Nadaraya-Watson estimator

$$\hat{f}_{NW}(c(I), y_{\mathcal{T}}(I))(l) := \sum_{i \in I} \frac{\omega_{il}}{\sum_{i \in I} \omega_{il}} y_{\mathcal{T}}(i)$$

446 where $\omega_{il} := \exp(-\gamma d(l, c(i))^2)$ and d is the Euclidean distance between centroid $c(i)$ and voxel with
 447 position l .

448 Several facets of the estimator are visible here. A smaller γ corresponds to a greater amount of
 449 smoothing, and the index set $I \subseteq \{1 : n\}$ generally depends on s and ν . Varying γ bridges between
 450 1-nearest neighbor prediction and averaging of all experiments in I . In Knox et al. (2019), I consisted
 451 of experiments sharing the same brain division, i.e. $I = I_m$, while restricting of index set to only
 452 include experiments with the same cell class gives the class-specific Cre-NW model. Despite this
 453 restriction, we fit γ by leave-one-out cross-validation for each m rather than a smaller subset like s or
 454 ν . That is,

$$\hat{\gamma}_m = \arg \min_{\gamma \in \mathbb{R}_{\geq 0}} \frac{1}{|\{s, \nu\}|} \sum_{s, \nu \in \{m, \mathcal{V}\}} \frac{1}{|I_s \cap I_\nu|} \sum_{i \in (I_s \cap I_\nu)} \ell(y_{\mathcal{T}}(i)), \hat{f}_{\mathcal{T}}(f_*(\mathcal{D}(\nu, s) \setminus i)). \quad (2)$$

⁴⁵⁵ *The Expected-Loss estimator* Besides location of the injection centroid, cell class also influences
⁴⁵⁶ projection. Thus, we introduce method for estimating the effect of Cre-distance, which we define as
⁴⁵⁷ the distance between the projections of the mean experiment of one (Cre,leaf) pair with another. This
⁴⁵⁸ method assigns a predictive weight to each pair of training points that depends both on their
⁴⁵⁹ centroid-distance and Cre-distance. This weight is determined by the expected prediction error of
⁴⁶⁰ each of the two feature types

⁴⁶¹ We define Cre-line behavior as the average regionalized projection of a Cre-line in a given structure
⁴⁶² (i.e. leaf). The vectorization of categorical information is known as **target encoding**

$$\bar{y}_{\mathcal{T},s,v} := \frac{1}{|I_s \cap I_v|} \sum_{i \in (I_s \cap I_v)} y_{\mathcal{T}}(i)$$

⁴⁶³ The Cre-distance is then define a **Cre-distance** in a leaf to be the distance between the target-encoded
⁴⁶⁴ projections of two Cre-lines. The relative predictive accuracy of Cre-distance and centroid distance is
⁴⁶⁵ determined by fitting a surface of projection distance as a function of Cre-distance and centroid
⁴⁶⁶ distance.

⁴⁶⁷ as determined by cross-validation. When we use shape-constrained B-splines to estimate this
⁴⁶⁸ weight, the weights then may be said to be used in a Nadaraya-Watson estimator.

⁴⁶⁹ For this reason, we call this the Expected Loss Estimator. The resulting weights are then utilized in a
⁴⁷⁰ Nadaraya-Watson estimator in a final prediction step. increase the effective sample size of our
⁴⁷¹ Nadaraya-Watson estimator,

⁴⁷² In mathematical terms, our full feature set consists of the centroid coordinates and the
⁴⁷³ target-encoded means of the combinations of virus type and injection-centroid structure. That is,

$$f_*(\mathcal{D}_i) = \{c(i), \{\bar{y}_{\mathcal{T},s,v} \forall v\}, y_{\mathcal{T}}(i)\}.$$

⁴⁷⁴ f^* is defined as in (2). The expected loss estimator is then

$$\hat{f}_{EL}(c(I), y_{\mathcal{T}}(I))(l, v) := \sum_{i \in I} \frac{v_{ilv}}{\sum_{i \in I} v_{ilv}} y_{\mathcal{T}}(i)$$

⁴⁷⁵ where

$$v_{ilv} := \exp(-\gamma g(d(l, c(i))^2, d(\bar{y}_{\mathcal{T},s,v}, \bar{y}_{\mathcal{T},s,v(i)})^2))$$

⁴⁷⁶ and s is the structure containing l .

⁴⁷⁷ The key step therefore is finding a suitable function g with which to weight the positional and Cre
⁴⁷⁸ information. Note that g must be a concave, non-decreasing function of its arguments with with
⁴⁷⁹ $g(0, 0) = 0$. Then, g defines a metric on the product of the metric spaces defined by experiment
⁴⁸⁰ centroid and target-encoded cre-line, and \hat{f}_{EL} is a Nadaraya-Watson estimator. A derivation of this
⁴⁸¹ fact is given later in this section.

⁴⁸² We therefore use a linear generalized additive model of shape-constrained B-splines to estimate g
⁴⁸³ (?). This is a method for generating a predictive model g that minimizes the loss of

$$\sum_{i, i' \in S} \| \|y_{\mathcal{T}}(i) - y_{\mathcal{T}}(i')\|_2 - \sum_{q=1}^Q \rho_q B_q(\|c(i') - c(i)\|_2, \|\bar{y}_{\mathcal{T}, s, v} - \bar{y}_{\mathcal{T}, s, v}(i)\|) \|_2$$

⁴⁸⁴ given the constraints on g . That is, given all pairs of experiments with injection centroid in the same
⁴⁸⁵ structure, g gives a prediction of the distance between their projections made using the distance
⁴⁸⁶ between the average behavior of their Cre-lines given their injection centroid, and the distance
⁴⁸⁷ between their injection centroids. In particular, g is the empirically best such function within the
⁴⁸⁸ class of B -splines, which Similarly to the Nadaraya-Watson model, we make the decision to fit a g
⁴⁸⁹ separately for each major brain division, and select $\hat{\gamma}$ as in 2. We set $Q = 10$ and leave validation of this
⁴⁹⁰ parameter, as well as the precise nature of the polynomial B-spline terms B_q out of the scope of this
⁴⁹¹ paper. Empirically this leads to a smooth surface using the pyGAM Python package (Servén D., n.d.).

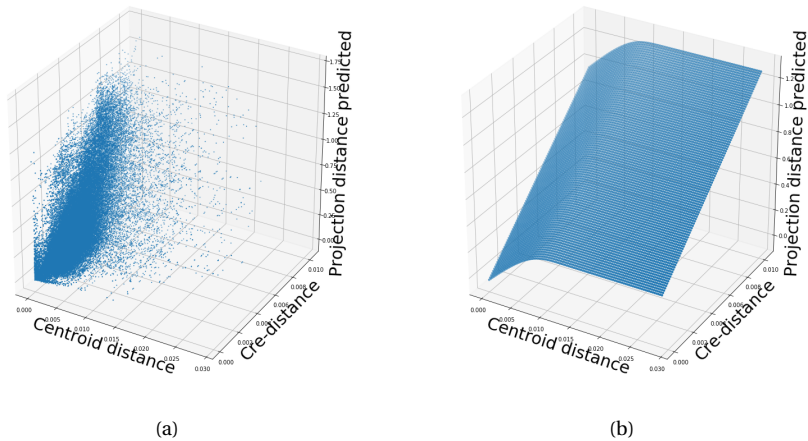


Figure 18: Fitting g . 18a Distribution of projection errors against centroid distance and cre-distance in Isocortex. 18b estimated \hat{g} using B-splines.

492 JUSTIFICATION OF SHAPE CONSTRAINT The shape-constrained expected-loss estimator introduced
 493 in this paper is, to our knowledge, novel. It should be considered an alternative method to the classic
 494 weighted kernel method. While we do not attempt a detailed theoretical study of this estimator, we do
 495 establish the need for the shape constraint in our spline estimator. Though this fact is probably well
 496 known, we prove a (slightly stronger) version here for completeness.

497 **Proposition 1.** *Given a collection of metric spaces X_1, \dots, X_n with metrics d_1, \dots, d_n (e.g. $d_{centroid}, d_{cre}$),
 498 and a function $f : (X_1 \times X_1) \dots \times (X_n \times X_n) = g(d_1(X_1 \times X_1), \dots, d_n(X_n \times X_n))$, then f is a metric if g is
 499 concave, non-decreasing and $g(d) = 0 \iff d = 0$.*

500 *Proof.* We show g satisfying the above properties implies that f is a metric.

- 501 ▪ The first property of a metric is that $f(x, x') = 0 \iff x = x'$. The left implication:
 502 $x = x' \implies f(x_1, x'_1, \dots, x_n, x'_n) = g(0, \dots, 0)$, since d are metrics. Then, since $g(0) = 0$, we have that
 503 $f(x, x') = 0$. The right implication: $f(x, x') = 0 \implies d = 0 \implies x = x'$ since d are metrics.
- 504 ▪ The second property of a metric is that $f(x, x') = f(x', x)$. This follows immediately from the
 505 symmetry of the d_i , i.e. $f(x, x') = f(x_1, x'_1, \dots, x_n, x'_n) = g(d_1(x_1, x'_1), \dots, d_n(x_n, x'_n)) =$
 506 $g(d_1(x'_1, x_1), \dots, d_n(x'_n, x_n)) = f(x'_1, x_1, \dots, x'_n, x_n) = f(x', x)$.
- 507 ▪ The third property of a metric is the triangle inequality: $f(x, x') \leq f(x, x^*) + f(x^*, x')$. To show this
 508 is satisfied for such a g , we first note that $f(x, x') = g(d(x, x')) \leq g(d(x, x^*) + d(x^*, x'))$ since g is
 509 non-decreasing and by the triangle inequality of d . Then, since g is concave,
 510 $g(d(x, x^*) + d(x^*, x')) \leq g(d(x, x^*)) + g(d(x^*, x')) = f(x, x^*) + f(x^*, x')$.

512 ***Setting a lower detection threshold***

513 The lower detection threshold of our approach is a complicated consequence of our experimental and
 514 analytical protocols. For example, the Nadaraya-Watson estimator is likely to generate many small
 515 false positive connections, since the projection of even a single experiment within the source region
 516 to a target will cause a non-zero connectivity in the Nadaraya-Watson weighted average. On the other
 517 hand, the complexities of the experimental protocol itself and the image analysis and alignment can
 518 also cause spurious signals. Therefore, it is of interest to establish a lower-detection threshold below
 519 which we have very little power-to-predict, and set estimated connectivities below this threshold to
 520 zero.

521 We set this threshold with respect to the sum of Type 1 and Type 2 errors

$$\iota = \sum_{i \in \mathcal{E}} 1_{y_{\mathcal{T}}^T(i)=0}^T 1_{\hat{f}_{\mathcal{T}}(\nu(i), c(i)) > \tau} + 1_{y_{\mathcal{T}}^T(i) > 0}^T 1_{\hat{f}_{\mathcal{T}}(\nu(i), c(i)) < \tau}.$$

522 We then select the τ that minimizes ι . Results for this approach are given in Supplemental Section 7.

523 ***Decomposing the connectivity matrix***

524 We utilize non-negative matrix factorization (NMF) to analyze the principal signals in our
 525 connectivity matrix. Here, we review this approach as applied to decomposition of the distal elements
 526 of the estimated connectivity matrix $\hat{\mathcal{C}}$ to identify q connectivity archetypes. Aside from the NMF
 527 program itself, the key elements are selection of the number of archetypes q and stabilization of the
 528 tendency of NMF to give random results over different initializations.

529 *Non-negative matrix factorization* As discussed in Knox et al. (2019), one of the most basic processes
 530 underlying the observed connectivity is the tendency of each source region to predominantly project
 531 to proximal regions. For example, the heatmap in Supplemental Figure 17 shows that the pattern of
 532 infrastructure distances resembles the connectivity matrix in 2. These connections are biologically
 533 meaningful, but also unsurprising, and their relative strength biases learned latent coordinate
 534 representations away from long-range structures. For this reason, we establish a $1500\mu\text{m}$ 'distal'
 535 threshold within which to exclude connections for our analysis.

536 Given a matrix $X \in \mathbb{R}_{\geq 0}^{a \times b}$ and a desired latent space dimension q , the non-negative matrix
 537 factorization is thus

$$\text{NMF}(\mathcal{C}, \lambda, q, \mathbf{1}_M) = \arg \min_{W \in \mathbb{R}_{\geq 0}^{S \times q}, H \in \mathbb{R}_{\geq 0}^{q \times T}} \frac{1}{2} \|\mathbf{1}_M \odot \mathcal{C} - WH\|_2^2 + \lambda(\|H\|_1 + \|W\|_1).$$

538 The mask $\mathbf{1}_M$ specifies this objective for detecting patterns in long-range connections. We note the
 539 existence of NMF with alternative norms for certain marginal distributions, but leave utilization of
 540 this approach for future work (Brunet, Tamayo, Golub, & Mesirov, 2004).

541 The mask $\mathbf{1}_M \in \{0, 1\}^{S \times T}$ serves two purposes. First, it enables computation of the NMF objective
 542 while excluding self and nearby connections. These connections are both strong and linearly
 543 independent, and so would unduly influence the *NMF* reconstruction error over more biologically
 544 interesting or cell-type dependent long-range connections. Second, it enables cross-validation based
 545 selection of the number of retained components.

546 *Cross-validating NMF* We review cross-validation for NMF following (?). In summary, a NMF model is
 547 first fit on a reduced data set, and an evaluation set is held out. After random masking of the
 548 evaluation set, the loss of the learned model is then evaluated on the basis of successful
 549 reconstruction of the held-out values. This procedure is performed repeatedly, with replicates of
 550 random masks at each tested dimensionality q . This determines the point past which additional
 551 hidden units provide no additional value for reconstructing the original signal.

552 The differentiating feature of cross-validation for NMF compared with supervised learning is the
 553 randomness of the masking matrix 1_M . Cross-validation for supervised learning generally leaves out
 554 entire observations, but this is insufficient for our situation. This is because, given W , our H is the
 555 solution of a regularized non-negative least squares optimization problem

$$H := \hat{e}_W(1_M \odot \mathcal{C}) = \arg \min_{\beta \in \mathbb{R}_{\geq 0}^{q \times T}} \|1_M \odot \mathcal{C} - W\beta\|_2^2 + \|\beta\|_1. \quad (3)$$

556 The negative effects of an overfit model can therefore be optimized away from on the evaluation set.

A standard solution is to generate uniformly random masks $1_{M(p)} \in \mathbb{R}^{S \times T}$ where

$$1_{M(p)}(s, t) \sim \text{Bernoulli}(p).$$

NMF is then performed using the mask $1_{M(p)}$ to get W . The cross-validation error is then

$$\epsilon_q = \frac{1}{R} \sum_{r=1}^R (\|1_{M(p)_r^c} \odot X - W(\hat{e}_W(1_{M(p)_r^c} \odot X))\|_2^2$$

where $1_{M(p)_r}^c$ is the binary complement of $1_{M(p)_r}$ and R is a number of replicates. Theoretically, the optimum number of components is then

$$\hat{q} = \operatorname{arg\,min}_q \epsilon_q.$$

557 *Stabilizing NMF* The NMF program is non-convex, and, empirically, individual replicates will not
 558 converge to the same optima. One solution therefore is to run multiple replicates of the NMF
 559 algorithm and cluster the resulting vectors. This approach raises the questions of how many clusters
 560 to use, and how to deal with stochasticity in the clustering algorithm itself. We address this issue
 561 through the notion of clustering stability (von Luxburg, 2010a).

The clustering stability approach is to generate L replicas of k-cluster partitions $\{C_{kl} : l \in 1 \dots L\}$ and then compute the average dissimilarity between clusterings

$$\xi_k = \frac{2}{L(L-1)} \sum_{l=1}^L \sum_{l'=1}^l d(C_{kl}, C_{kl'}).$$

Then, the optimum number of clusters is

$$\hat{k} = \arg \min_k \xi_k.$$

562 A review of this approach is found in von Luxburg (2010b). Intuitively, archetype vectors that cluster
 563 together frequently over clustering replicates indicate the presence of a stable clustering. For d , we
 564 utilize the adjusted Rand Index - a simple dissimilarity measure between clusterings. Note that we
 565 expect to select slightly more than the q components suggested by cross-validation, since archetype
 566 vectors which appear in one NMF replicate generally should appear in others. We then select the q
 567 clusters with the most archetype vectors - the most stable NMF results - and take the median of each
 568 cluster to create a sparse representative archetype Kotliar et al. (2019); Wu et al. (2016). We then find
 569 the according H using Program 3. Experimental results for these cross-validation and stability
 570 selection approaches are given in Supplemental Section 7.

7 SUPPLEMENTAL EXPERIMENTS

571 Setting detection threshold τ

572 We give results on the false detection rate at different limits of detection. These conclusively show that
 573 10^{-6} is the good threshold for our normalized data.

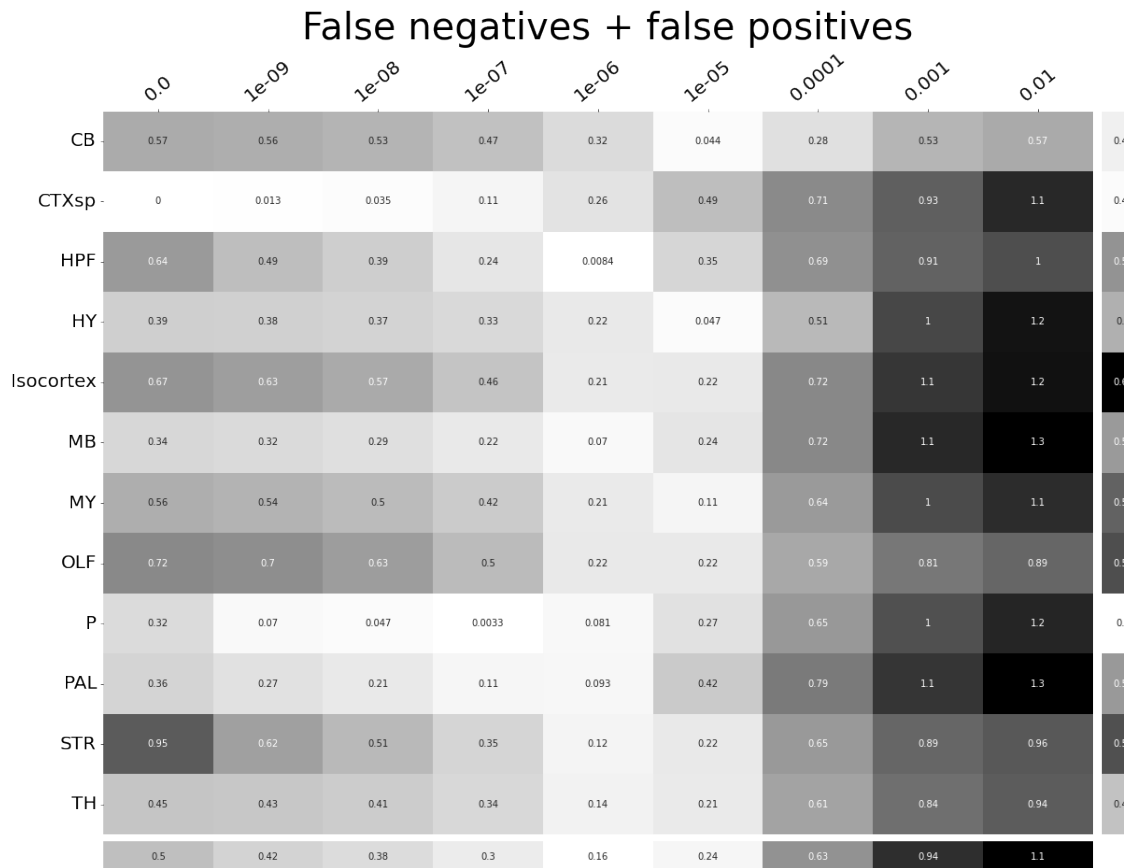


Figure 19: τ at different limits of detection in different major structures. 10^{-6} is the optimal detection threshold.

574 ***Loss subsets***

575 We report model accuracies for our *EL* model by neuron class and structure. These expand upon the
 576 results in Table 5 and give more specific information about the quality of our estimates. CTXsp is
 577 omitted due to the small nature of the evaluation set.

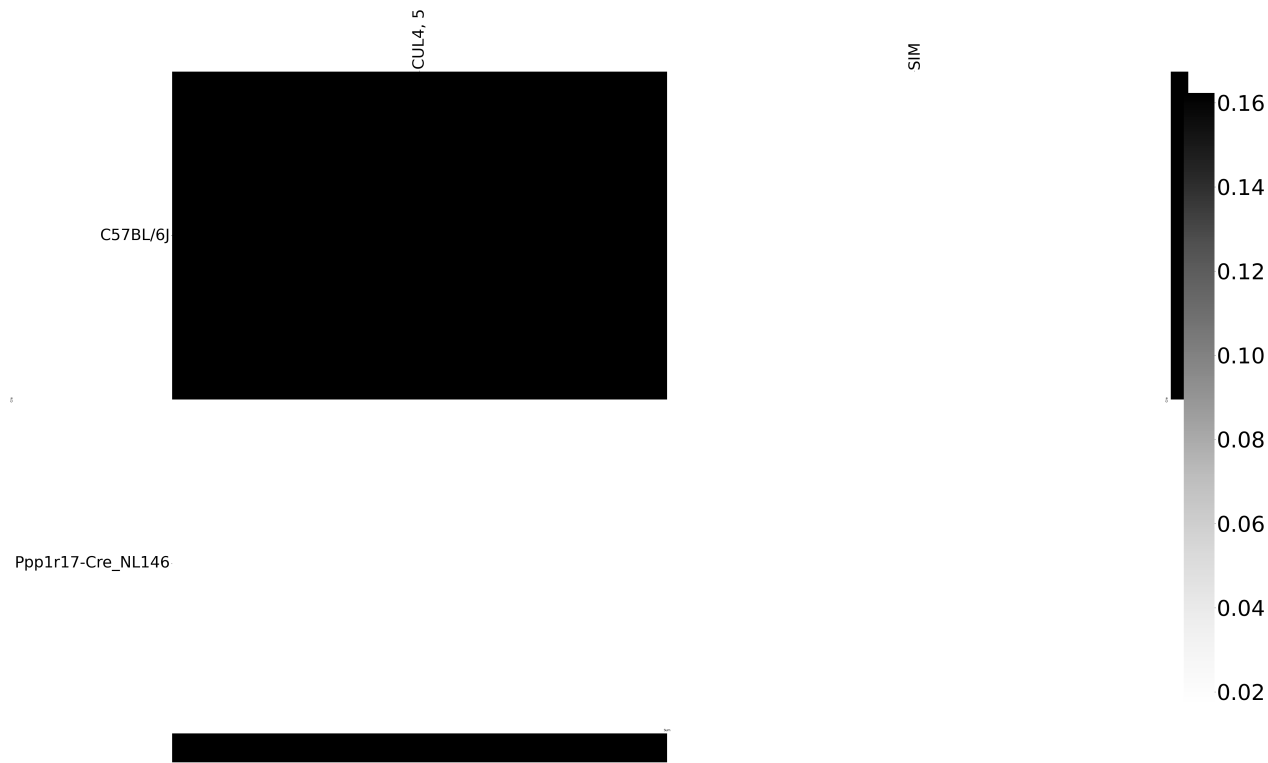


Figure 20: Weighted loss for cre-leaf combinations in CB. Missing values are omitted. Row and column averages are also plotted.

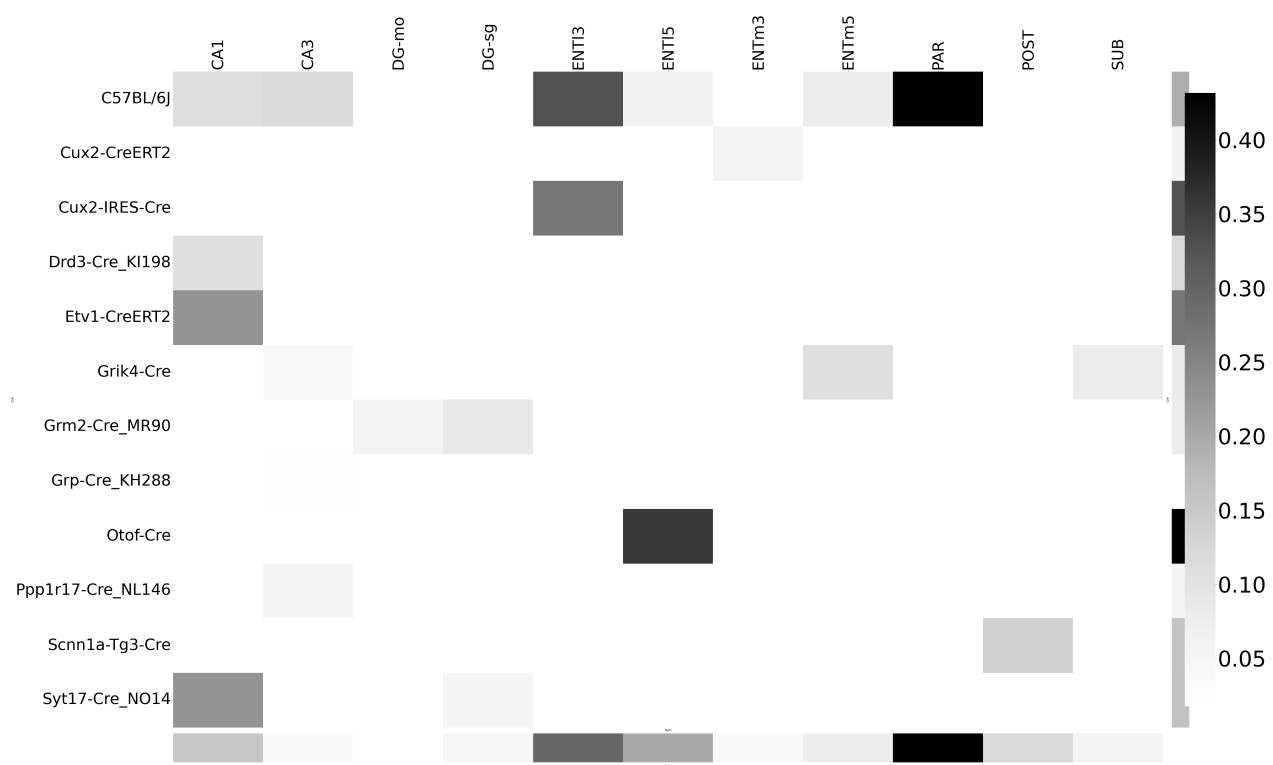


Figure 21: Weighted loss for cre-leaf combinations in HPF. Missing values are omitted. Row and column averages are also plotted.

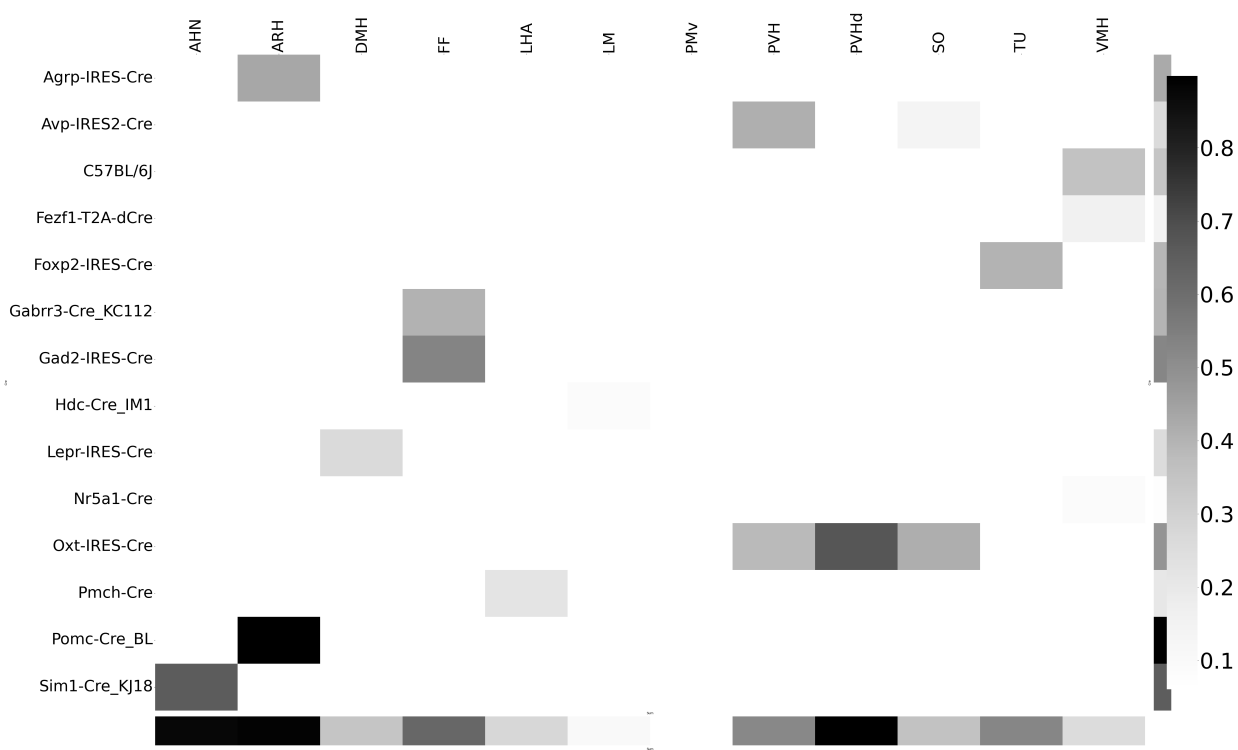


Figure 22: Weighted loss for cre-leaf combinations in HY. Missing values are omitted. Row and column averages are also plotted.

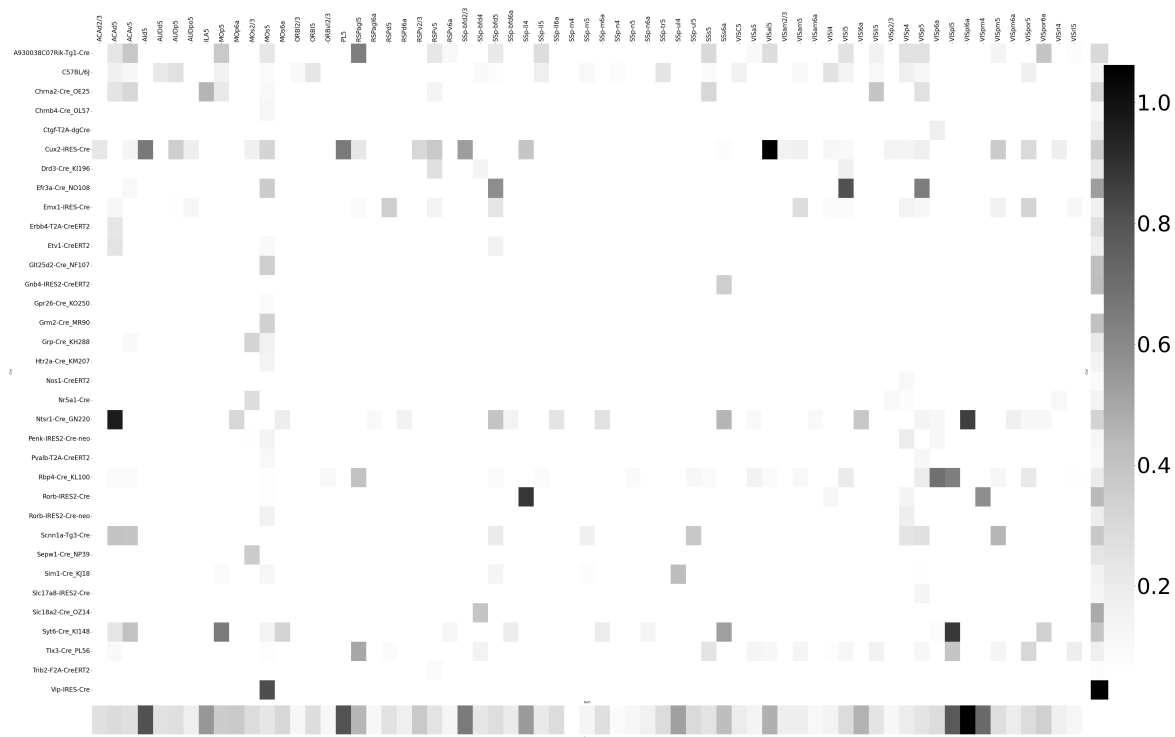


Figure 23: Weighted loss for cre-leaf combinations in Isocortex. Missing values are omitted. Row and column averages are also plotted.

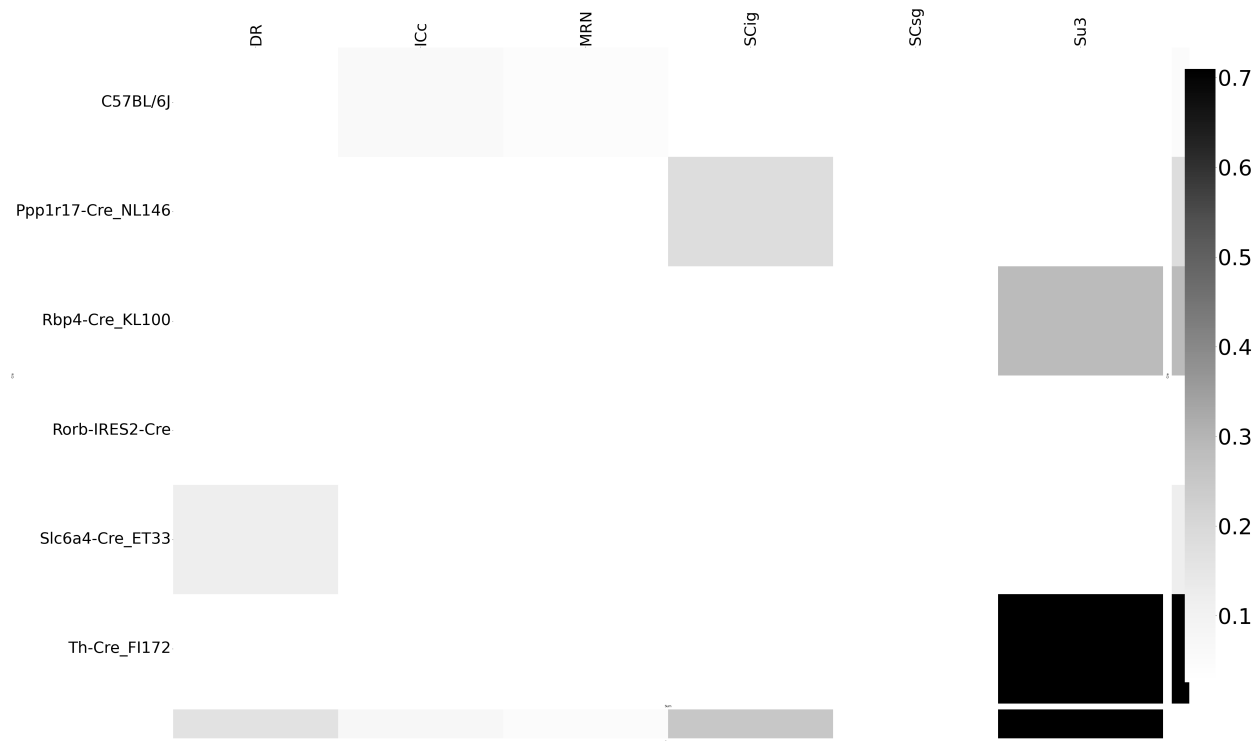


Figure 24: Weighted loss for cre-leaf combinations in MB. Missing values are omitted. Row and column averages are also plotted.

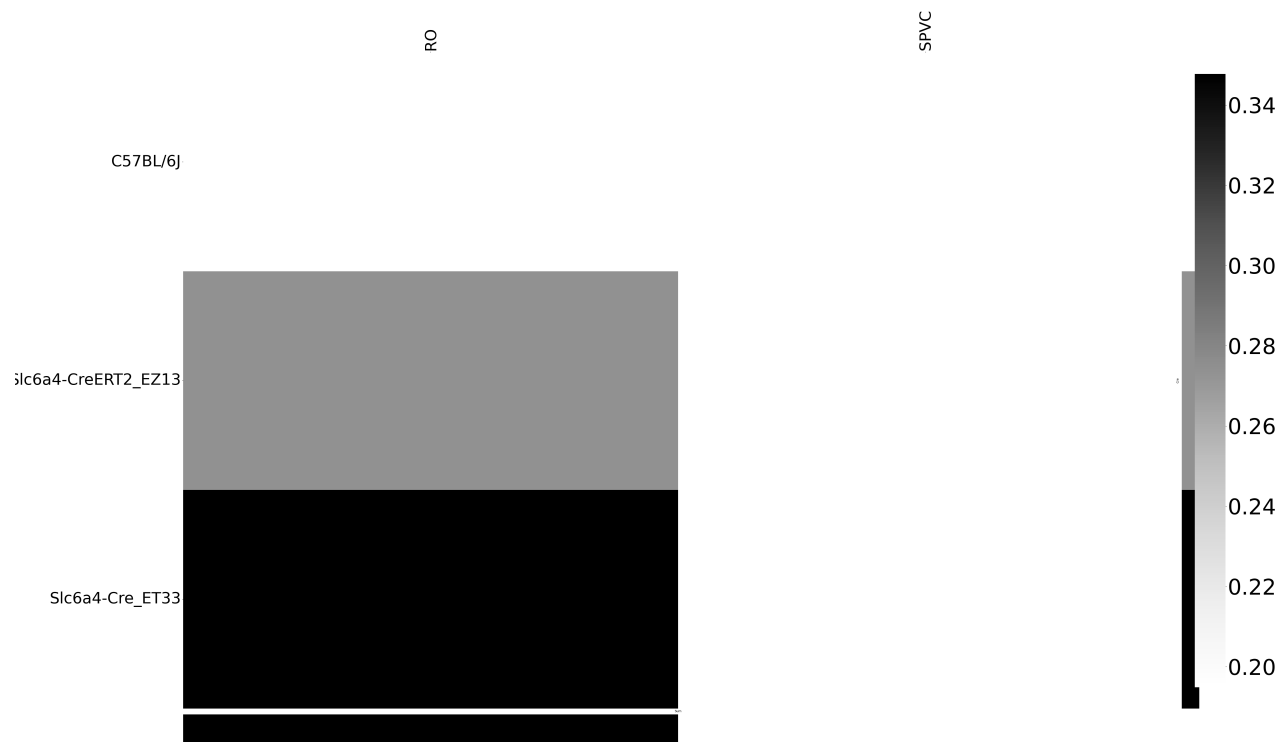


Figure 25: Weighted loss for cre-leaf combinations in MY. Missing values are omitted. Row and column averages are also plotted.

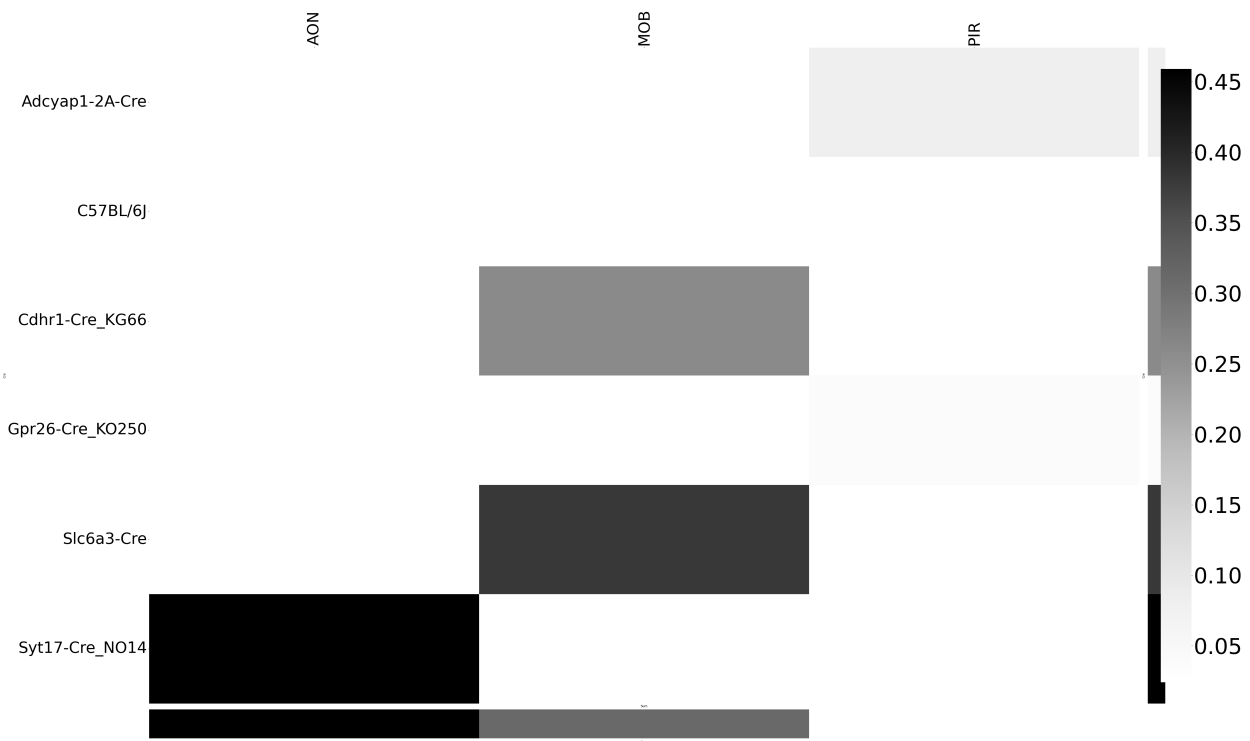


Figure 26: Weighted loss for cre-leaf combinations in OLF. Missing values are omitted. Row and column averages are also plotted.

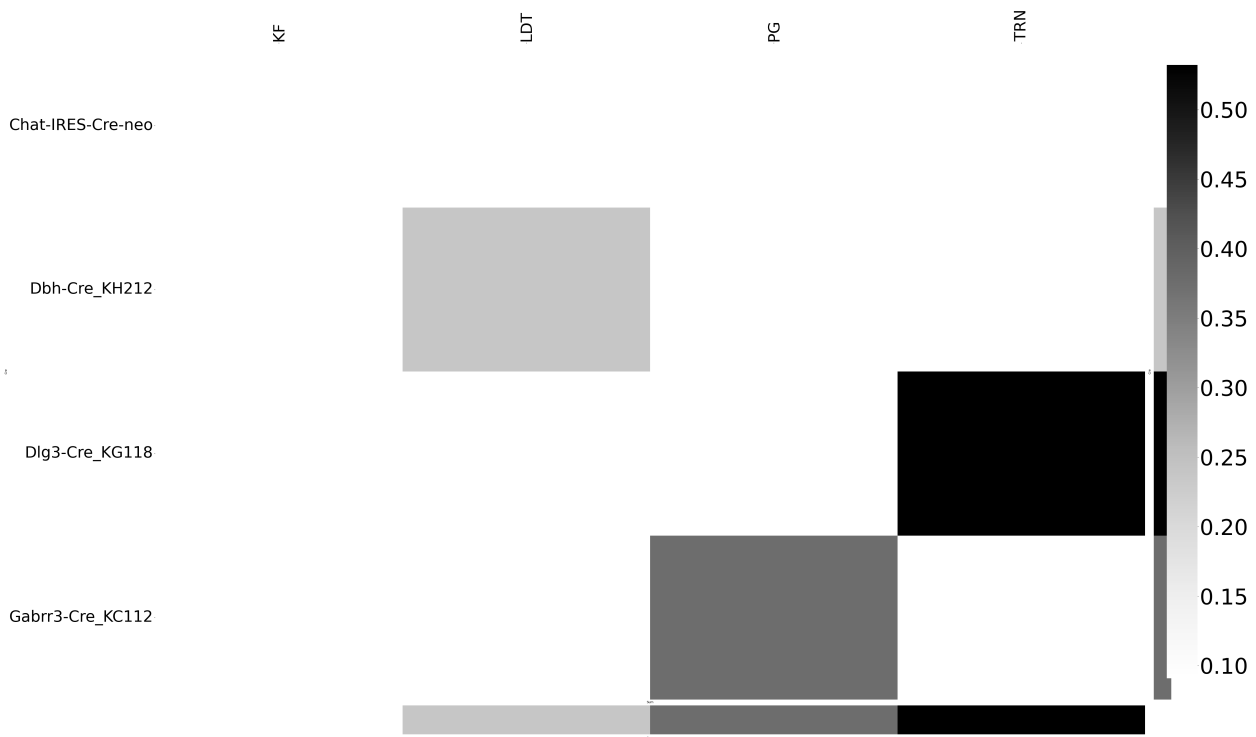


Figure 27: Weighted loss for cre-leaf combinations in P. Missing values are omitted. Row and column averages are also plotted.

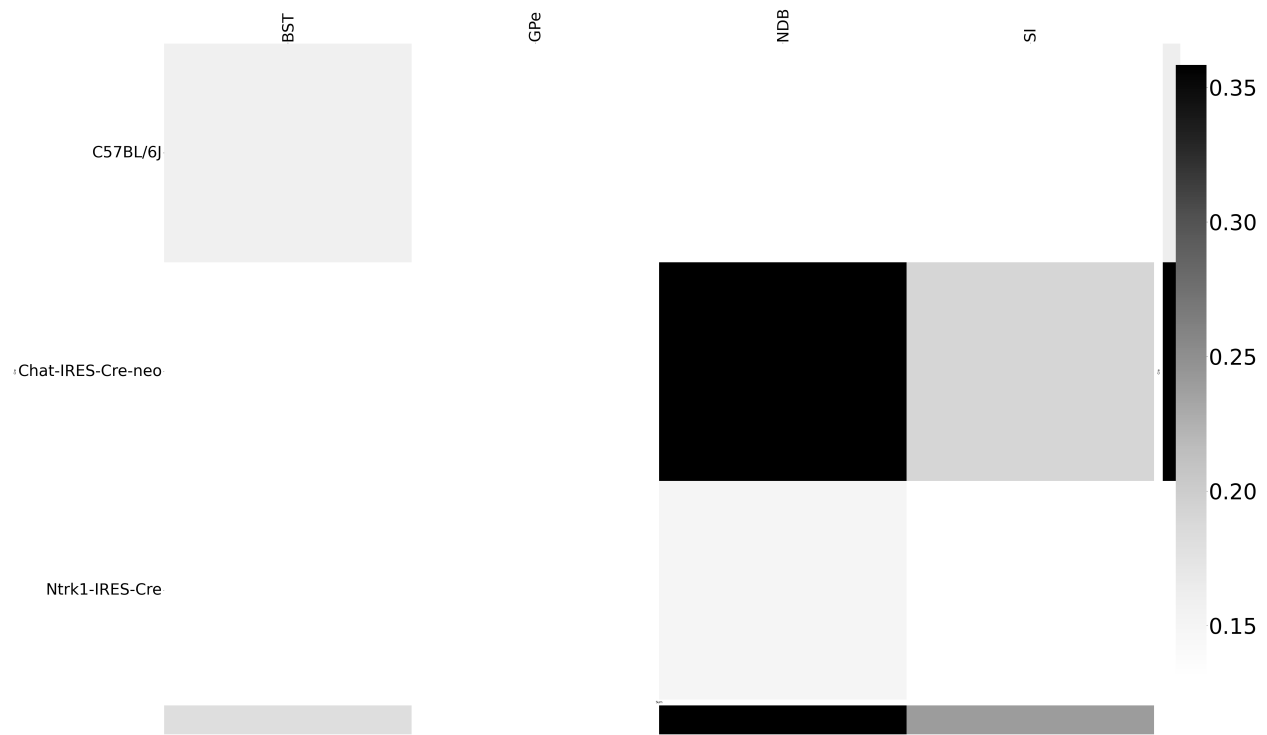


Figure 28: Weighted loss for cre-leaf combinations in PAL. Missing values are omitted. Row and column averages are also plotted.

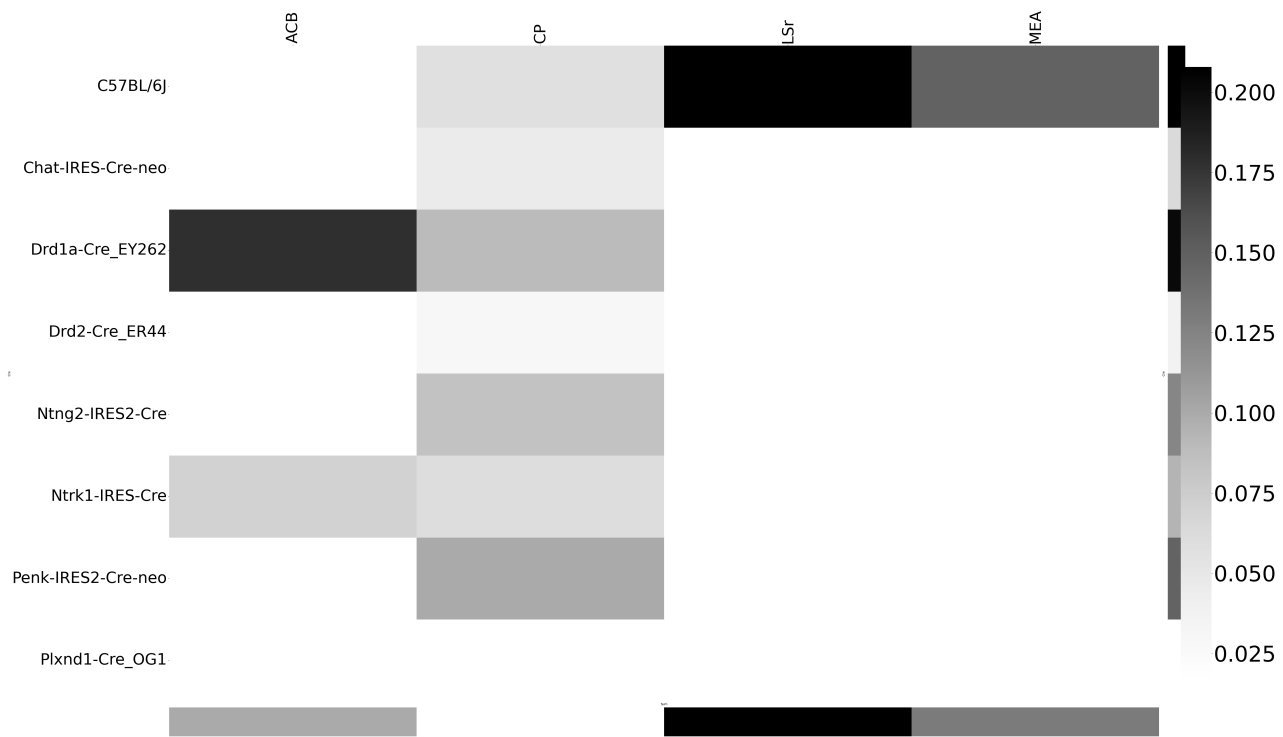


Figure 29: Weighted loss for cre-leaf combinations in STR. Missing values are omitted. Row and column averages are also plotted.

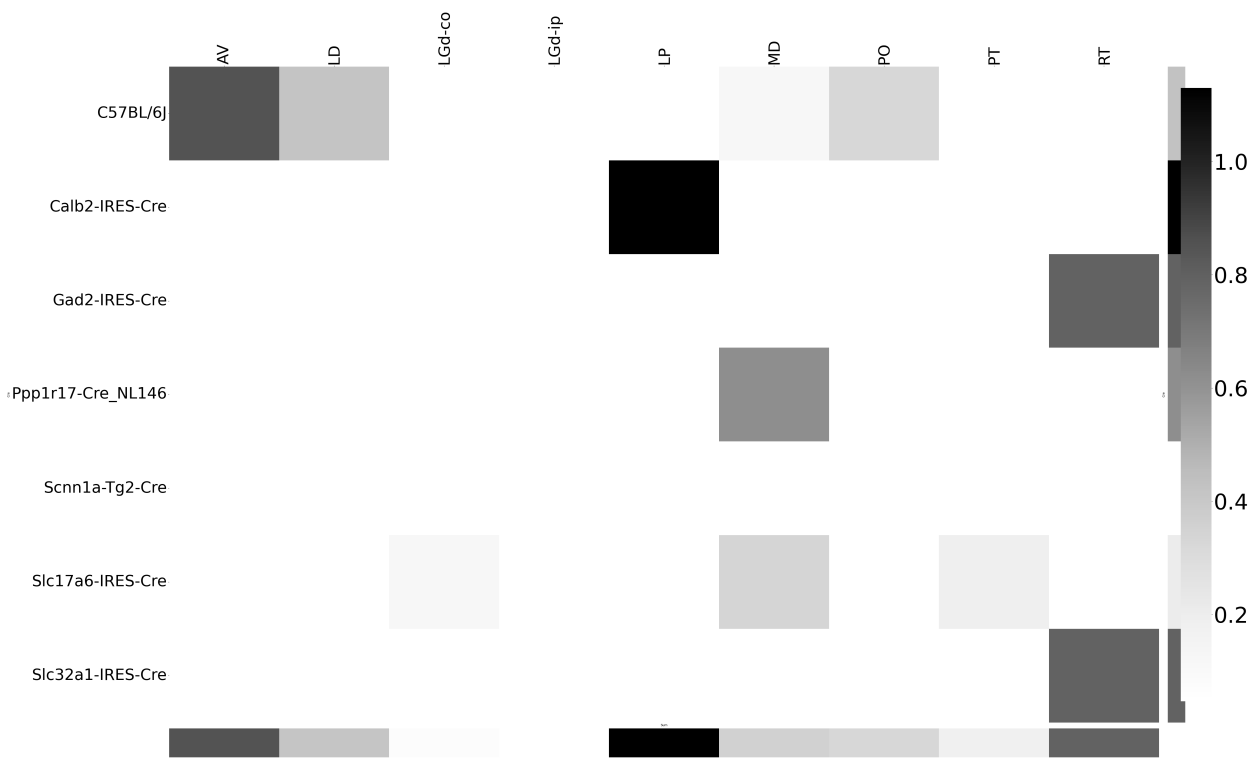


Figure 30: Weighted loss for cre-leaf combinations in TH. Missing values are omitted. Row and column averages are also plotted.

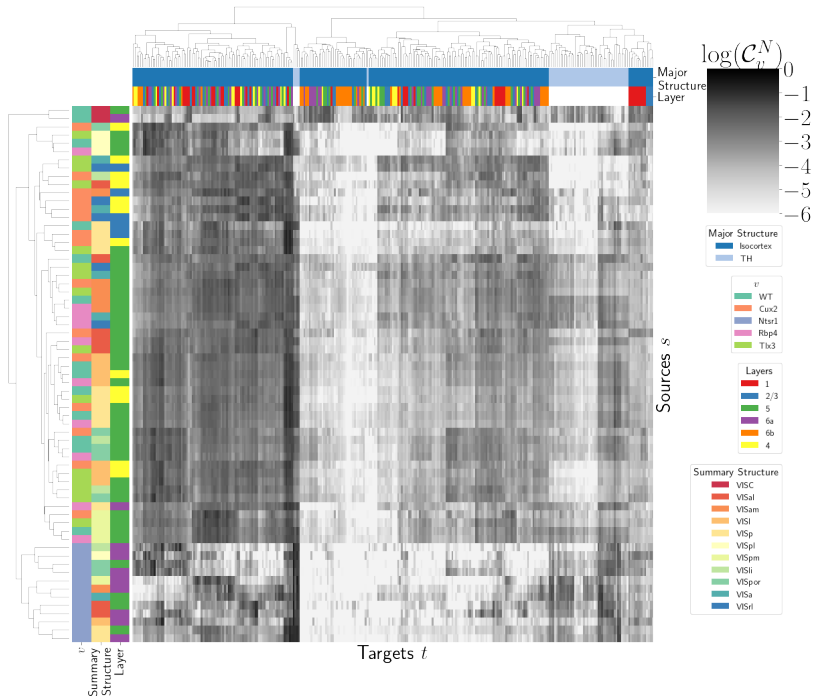


Figure 31: ?? Hierarchical clustering of connectivity strengths from visual cortex cell-types to cortical and thalamic targets. Cre-line, summary structure, and layer are labelled on the sources. Major brain division and layer are labelled on the targets.

578 **Cell-type specificity**

579 **Matrix Factorization**

580 We give additional results on the generation of the archetypal connectome patterns. These consist of
 581 cross-validation selection of q , the number of latent components, stability analysis, and visualization
 582 of the reconstructed wild-type connectivity.

583 **Cross-validation** We set $\alpha = 0.002$ and run Program 2 on \mathcal{C}_{wt} . We use a random mask with $p = .3$ to
 584 evaluate prediction accuracy of models trained on the unmasked data on the masked data. To
 585 account for stochasticity in the NMF algorithm, we run $R = 8$ replicates at each potential dimension q .
 586 This selects $\hat{q} = 60$.

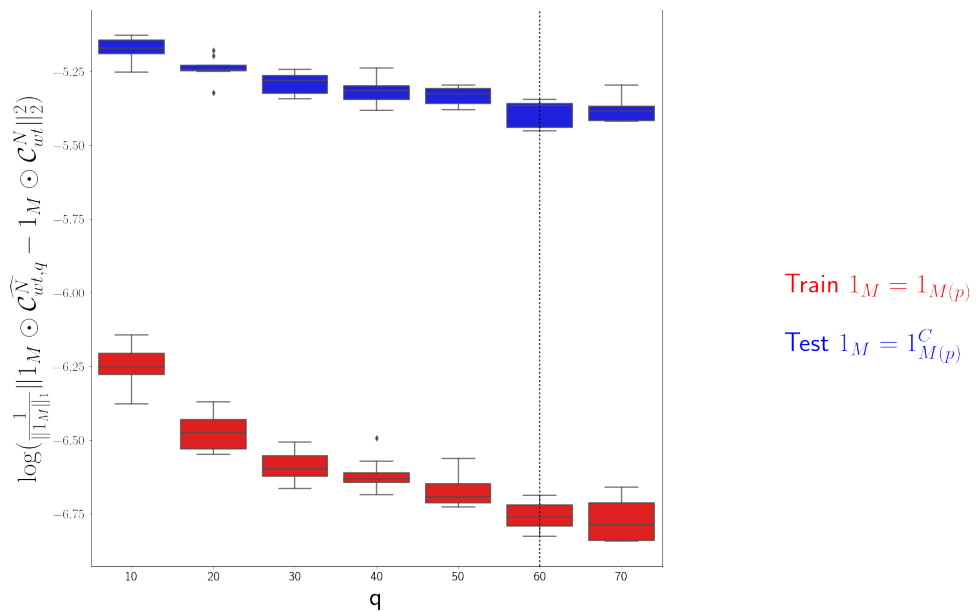


Figure 32: Train and test error using NMF decomposition.

587 *Stability* For the purposes of visualization and interpretability, we restrict to a $q = 15$ component
 588 model. To address the instability of the NMF algorithm in identifying components, we $k - means$
 589 cluster components over $R = 10$ replicates with $k \in \{10, 15, 20, 25, 30\}$. Since the clustering is itself
 590 unstable, we repeat the clustering 25 times and select the k with the largest Rand index.

591 q	10.000000	20.000000	30.000000	40.000000	50.000000
Rand index	0.772544	0.844981	0.932957	0.929827	0.885862

592 Since k -means is most stable at $k = 30$, we cluster the $qR = 150$ components into 30 clusters and
 593 select the 15 clusters appearing in the most replicates.

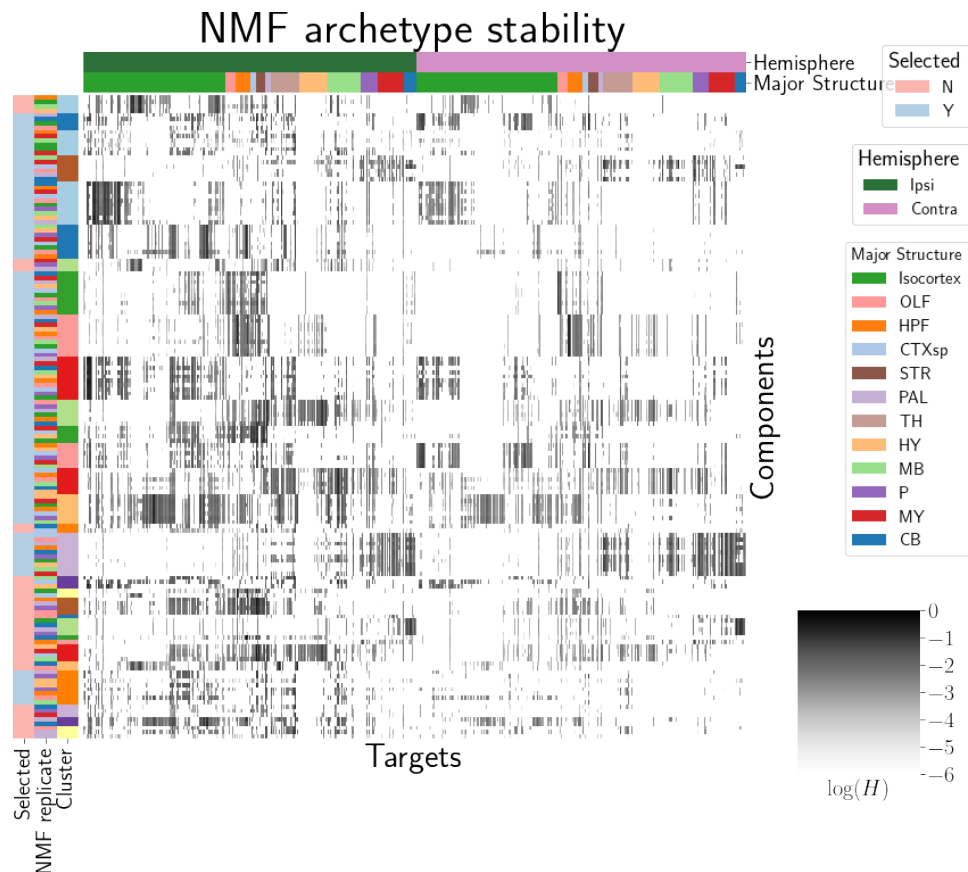


Figure 33: Stability of NMF results across replicates. Replicate and NMF component are shown on rows. Components that are in the top 15 are also indicated.

594 These are the components whose medians are plotted in Figure 4a.

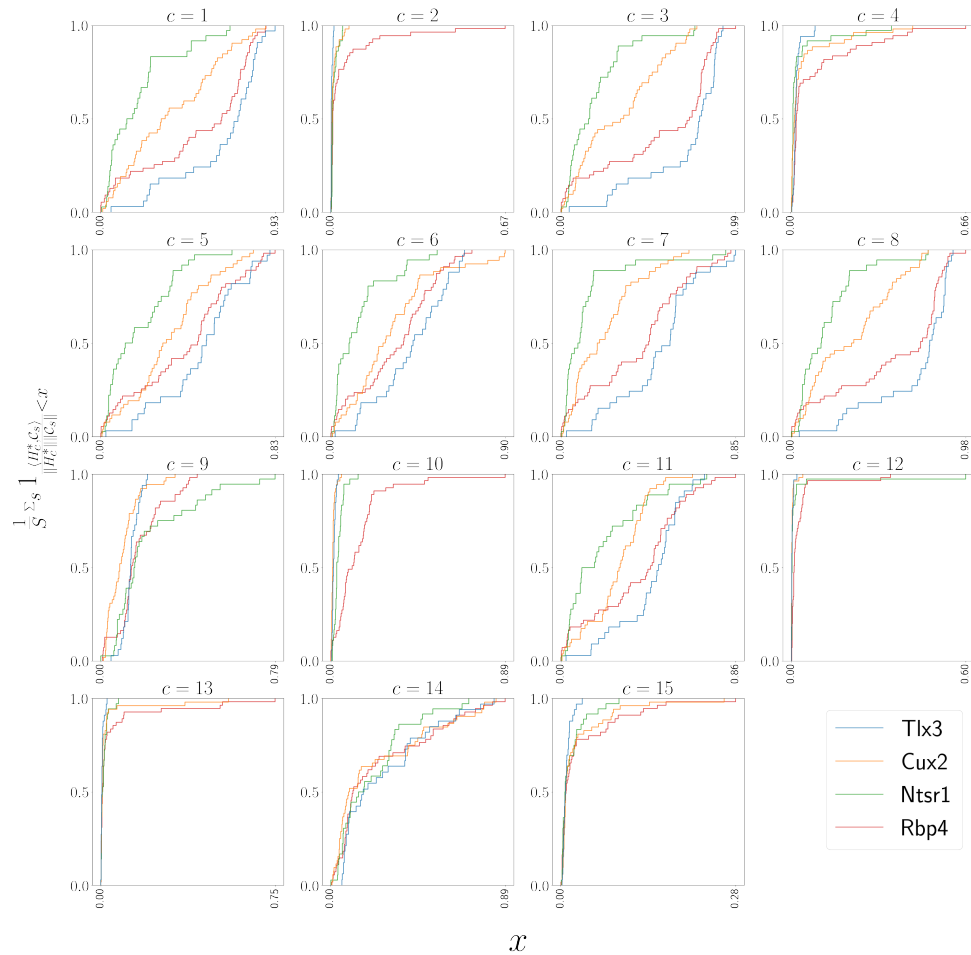


Figure 34: Empirical cumulative distributions of cosine similarities between source structures and connectivity components for four different Cre-lines.

595 *Association with Cre-line*

8 COMPETING INTERESTS

⁵⁹⁶ This is an optional section. If you declared a conflict of interest when you submitted your manuscript,
⁵⁹⁷ please use this space to provide details about this conflict.

598

599

REFERENCES

600

601 Brunet, J.-P., Tamayo, P., Golub, T. R., & Mesirov, J. P. (2004). Metagenes and molecular pattern discovery using matrix
602 factorization. *Proc. Natl. Acad. Sci. U. S. A.*, 101(12), 4164–4169.

603 Chamberlin, N. L., Du, B., de Lacalle, S., & Saper, C. B. (1998). Recombinant adeno-associated virus vector: use for
604 transgene expression and anterograde tract tracing in the CNS. *Brain Res.*, 793(1-2), 169–175.

605 Daigle, T. L., Madisen, L., Hage, T. A., Valley, M. T., Knoblich, U., Larsen, R. S., ... Zeng, H. (2018). A suite of transgenic
606 driver and reporter mouse lines with enhanced Brain-Cell-Type targeting and functionality. *Cell*, 174(2), 465–480.e22.

607 Gao, Y., Zhang, X., Wang, S., & Zou, G. (2016). Model averaging based on leave-subject-out cross-validation. *J. Econom.*,
608 192(1), 139–151.

609 Harris, J. A., Mihalas, S., Hirokawa, K. E., Whitesell, J. D., Choi, H., Bernard, A., ... Zeng, H. (2019). Hierarchical
610 organization of cortical and thalamic connectivity. *Nature*, 575(7781), 195–202.

611 Harris, J. A., Oh, S. W., & Zeng, H. (2012). Adeno-associated viral vectors for anterograde axonal tracing with fluorescent
612 proteins in nontransgenic and cre driver mice. *Curr. Protoc. Neurosci., Chapter 1, Unit 1.20.1–18*.

613 Harris, K. D., Mihalas, S., & Shea-Brown, E. (2016). Nonnegative spline regression of incomplete tracing data reveals high
614 resolution neural connectivity.

615 Huang, K. W., Ochandarena, N. E., Philson, A. C., Hyun, M., Birnbaum, J. E., Cicconet, M., & Sabatini, B. L. (2019).
616 Molecular and anatomical organization of the dorsal raphe nucleus. *Elife*, 8.

617 Jeong, M., Kim, Y., Kim, J., Ferrante, D. D., Mitra, P. P., Osten, P., & Kim, D. (2016). Comparative three-dimensional
618 connectome map of motor cortical projections in the mouse brain. *Sci. Rep.*, 6, 20072.

619 Knox, J. E., Harris, K. D., Graddis, N., Whitesell, J. D., Zeng, H., Harris, J. A., ... Mihalas, S. (2019). High-resolution
620 data-driven model of the mouse connectome. *Netw Neurosci*, 3(1), 217–236.

621 Kotliar, D., Veres, A., Nagy, M. A., Tabrizi, S., Hodis, E., Melton, D. A., & Sabeti, P. C. (2019). Identifying gene expression
622 programs of cell-type identity and cellular activity with single-cell RNA-Seq. *Elife*, 8.

- 623 Li, X., Yu, B., Sun, Q., Zhang, Y., Ren, M., Zhang, X., ... Qiu, Z. (2018). Generation of a whole-brain atlas for the
 624 cholinergic system and mesoscopic projectome analysis of basal forebrain cholinergic neurons. *Proc. Natl. Acad. Sci.*
 625 *U. S. A.*, 115(2), 415–420.
- 626 Lotfollahi, M., Naghipourfar, M., Theis, F. J., & Alexander Wolf, F. (2019). Conditional out-of-sample generation for
 627 unpaired data using trVAE.
- 628 Muzerelle, A., Scotto-Lomassese, S., Bernard, J. F., Soiza-Reilly, M., & Gaspar, P. (2016). Conditional anterograde tracing
 629 reveals distinct targeting of individual serotonin cell groups (B5-B9) to the forebrain and brainstem. *Brain Struct.*
 630 *Funct.*, 221(1), 535–561.
- 631 Oh, S. W., Harris, J. A., Ng, L., Winslow, B., Cain, N., Mihalas, S., ... Zeng, H. (2014). A mesoscale connectome of the
 632 mouse brain. *Nature*, 508(7495), 207–214.
- 633 Ren, J., Friedmann, D., Xiong, J., Liu, C. D., Ferguson, B. R., Weerakkody, T., ... Luo, L. (2018). Anatomically defined and
 634 functionally distinct dorsal raphe serotonin sub-systems. *Cell*, 175(2), 472–487.e20.
- 635 Ren, J., Isakova, A., Friedmann, D., Zeng, J., Grutzner, S. M., Pun, A., ... Luo, L. (2019). Single-cell transcriptomes and
 636 whole-brain projections of serotonin neurons in the mouse dorsal and median raphe nuclei. *Elife*, 8.
- 637 Saul, L. K., & Roweis, S. T. (2003). Think globally, fit locally: Unsupervised learning of low dimensional manifolds. *J.*
 638 *Mach. Learn. Res.*, 4(Jun), 119–155.
- 639 Servén D., B. C. (n.d.). *pygam: Generalized additive models in python*.
- 640 von Luxburg, U. (2010a). Clustering stability: An overview.
- 641 von Luxburg, U. (2010b). Clustering stability: An overview.
- 642 Watson, C., Paxinos, G., & Puelles, L. (2012). The mouse nervous system..
- 643 Wu, S., Joseph, A., Hammonds, A. S., Celiker, S. E., Yu, B., & Frise, E. (2016). Stability-driven nonnegative matrix
 644 factorization to interpret spatial gene expression and build local gene networks. *Proc. Natl. Acad. Sci. U. S. A.*, 113(16),
 645 4290–4295.
- 646 Zaborszky, L., Csordas, A., Mosca, K., Kim, J., Gielow, M. R., Vadasz, C., & Nadasdy, Z. (2015). Neurons in the basal
 647 forebrain project to the cortex in a complex topographic organization that reflects corticocortical connectivity

648 patterns: an experimental study based on retrograde tracing and 3D reconstruction. *Cereb. Cortex*, 25(1), 118–137.

9 TECHNICAL TERMS

649 **Technical Term** a key term that is mentioned in an NETN article and whose usage and definition may
650 not be familiar across the broad readership of the journal.

651 **Cre-line** Refers to the combination of cre-recombinase expression in transgenic mouse and
652 cre-induced promotion in the vector that induces labelling of cell-class specific projection.

653 **Cell class** The projecting neurons targeted by a particular cre-line

654 **Structural connectivities** connectivity between structures

655 **Voxel** A $100\mu m$ cube of brain.

656 **Structural connection tensor** Connectivities between structures given a neuron class

657 **dictionary-learning** A family of algorithms for finding low-dimensional data representations.

658 **Shape constrained estimator** A statistical estimator that fits a function of a particular shape (e.g.
659 monotonic increasing, convex).

660 **Nadaraya-Watson** A simple smoothing estimator.

661 **Connectivity archetypes** Typical connectivity patterns

662 **Expected loss** Our new estimator that weights different features by their estimated predictive
663 power.